

X-rays and regions of star formation: a combined ROSAT-HRI/near-to-mid IR study of the ρ Oph dark cloud^{*}

N. Grosso^{1,2}, T. Montmerle¹, S. Bontemps³, P. André¹, and E.D. Feigelson⁴

¹ Service d'Astrophysique, CEA/DSM/DAPNIA, CEA-Saclay, F-91191 Gif-sur-Yvette Cedex, France

² Max-Planck-Institut für extraterrestrische Physik, Giessenbachstraße 1, D-85740 Garching, Germany

³ Observatoire de Bordeaux, BP 89, F-33270 Floirac, France

⁴ Departement of Astronomy and Astrophysics, Pennsylvania State University, University Park, PA 16802, USA

Received / Accepted

Abstract. We have obtained two deep exposures of the ρ Oph cloud core region with the *ROSAT High Resolution Imager*. The improved position accuracy ($1''$ – $6''$) with respect to previous recent X-ray observations (*ROSAT PSPC*, and *ASCA*) allows us to remove positional ambiguities for the detected sources. We also cross-correlate the X-ray positions with IR sources found in the *ISOCAM* survey of the same region at 6.7 and 14.3 μm , in addition to sources (optical and IR) known from ground-based observations, which are young stars (T Tauri stars, with and without circumstellar disks, and protostars). We thus obtain the best-studied sample of X-ray emitting stars in a star-forming region (63 X-ray sources detected, and 55 identified).

We find that there is no statistically significant difference between the X-ray luminosity functions of *HRI*-detected Class II and Class III sources, i.e., T Tauri stars with and without disks, confirming that the contribution of these disks to X-ray emission (for instance by magnetic reconnection between the star and the disk), or to X-ray absorption, must be small.

X-ray variability of T Tauri stars can be studied by comparing the *HRI* data with the previously obtained *PSPC* data, but also using the fact that some *HRI* observations were done at different epochs. The resulting statistics show that most of the sources are variable, and that their variability is consistent with a solar-like (hence magnetic) flare origin.

We use the information given both by the *ISOCAM* survey and by our *HRI* deep exposure to study the T Tauri star population of the ρ Oph dense cores. We confirm that essentially all Class II and Class III sources (embedded T Tauri stars) are X-ray emitters, and that a strong correlation exists between their X-ray luminosity, L_X , and

their stellar luminosity, L_* , with $L_X/L_* \sim 10^{-4}$. Most of the new *ISOCAM* Class II sources are not detected, however, which we explain by the fact that their X-ray luminosities “predicted” on the basis of this correlation are too faint to be detected by the *HRI*.

We predict that ~ 40 unknown faint or embedded Class III sources remain to be discovered in X-rays in the *HRI/ISOCAM* overlapping area, down to a limit of $L_X \sim 3 \times 10^{28} \text{ erg s}^{-1}$. We show that the bulk of these unknown Class III sources should be made of low- to very low-mass stars ($M_* < 0.1$ – $0.6 M_\odot$). Prospects for future detections with *XMM-Newton* and *Chandra* are discussed.

Key words: (Galaxy:) open clusters and associations: individual: ρ Ophiuchi cluster – stars: pre-main sequence – stars: formation – X-rays: stars – infrared: stars

1. Introduction

The ρ Ophiuchi dark cloud complex is one of the nearest active site of low-mass star formation (see Wilking 1992 for a review). It is composed of two main dark clouds, L1688 and L1689, from which filamentary dark clouds, called streamers, extend to the north-east over tens of parsecs (e.g., Loren 1989; de Geus et al. 1990). The main star formation activity is observed in the westernmost dark cloud, L1688, which shows a rich cluster of low mass young stellar objects (YSO) around two dense molecular cores, “core A” and “core F” in the terminology of Loren (1989) and Loren et al. (1990).

The distance to the molecular complex remains somewhat controversial (see Wilking 1992), with a usually adopted distance $d \sim 160$ pc from the Sun. From *Hipparcos* parallaxes and Tycho B–V colors of classes V and III stars, Knude & Høg (1998) have detected at $d = 120$ pc an abrupt rise of the reddening as expected from a molecular cloud. Based on the *Hipparcos* positions, proper motions, and parallaxes, de Zeeuw et al. (1999) gives $d = 145 \pm 2$ pc

Send offprint requests to: N. Grosso, ngrosso@xray.mpe.mpg.de

^{*} Table A1, Fig. A1, Table B1 and Fig. B1 are only available in the on-line edition of the Journal (Table B1 is also available at the CDS).

for the mean distance of the Upper Scorpius OB association. We adopt $d = 140$ pc in this article, instead of 160 pc used in our previous work.

From infrared (IR) observations of star-forming regions, Lada and collaborators (e.g. Lada 1987; Wilking, Lada, & Wilking 1989, hereafter WLY) introduced an IR classification and distinguished different stages of evolution of young stellar objects (YSO). This classification was subsequently revisited by André & Montmerle (1994, hereafter AM) to incorporate results of millimeter continuum studies on circumstellar dust. The IR sources are classified in three classes, according to their spectral energy distributions (SEDs). This classification, initially defined empirically, is now well understood in terms of evolution of low-mass stars at their earliest stages. Submillimeter observations led to the discovery of cold objects, younger than the IR sources, and thus to the introduction of a fourth class named “Class 0” (André et al. 1993, 2000). Class 0 sources are very young protostars, peaking in the submillimeter range, at the beginning of the main accretion phase. Class I sources are evolved IR protostars, optically invisible, in the late accretion phase. Class II sources are YSO surrounded by optically thick circumstellar disks. Class III sources are YSO with an optically thin circumstellar disk or no circumstellar disk. Studies of optically visible YSO, T Tauri stars, led to another classification based on the H_α line, which separates “classical” T Tauri stars (CTTS) from “weak-line” T Tauri stars (WTTS) according to their equivalent width in emission, with a boundary at $EW[H_\alpha] \sim 5 - 20 \text{ \AA}$, depending on the spectral type (Martín 1997). CTTS and WTTS are usually taken to be identical to Class II and Class III sources respectively, on the basis of their IR SED (see AM for a discussion about these two classifications). We will associate in this article Class II (Class III) sources with CTTS (WTTS).

Several ground-based near-IR surveys (e.g. Wilking et al. 1989; Greene et al. 1994, hereafter GWAYL; Barsony et al. 1997, hereafter BKL; and references therein) discovered in a ≈ 1 square degree area around the densest regions (with survey completeness limit down to $K \sim 14$), ~ 100 low-luminosity embedded sources. More recently, the *ISOCAM* camera on-board the *Infrared Space Observatory* satellite imaged a half square degree centered on L1688 in the mid-IR (LW2 and LW3 filters, respectively centered at $6.7 \mu\text{m}$ and $14.3 \mu\text{m}$ – *ISOCAM* central programme surveys by Nordh et al.; see Abergel et al. 1996), and recognized 68 new faint young stars with infrared excess (Bontemps et al. 2000).

Near-IR spectroscopy has been used to determine spectral types of an increasingly large number of ρ Oph YSO (see the pioneering works of Greene & Meyer 1995, and Greene & Lada 1996). Recently, Luhman & Rieke (1999) obtained K -band spectroscopy for ~ 100 sources, combining a magnitude-limited sample in the cloud core ($K \leq 12$)

with a representative population from the outer region of the cluster ($K \leq 11$).

The ρ Oph dark cloud YSO have also been extensively studied in X-rays. Early observations with the *Einstein Observatory* satellite showed that at the T Tauri star stage YSO are bright and variable X-ray emitters in the 0.2–4 keV energy band (Montmerle et al. 1983). When the S/N ratio is sufficient large, their X-ray spectra can be fitted by a thin thermal model, with temperatures ≈ 1 keV and absorption column densities $N_H \sim 10^{20} - 10^{22} \text{ cm}^{-2}$. Variability studies and modeling led to explain the X-ray emission in terms of bremsstrahlung from a hot ($T_X \sim 10^7$ K) plasma trapped in very large magnetic loops, in other words in terms of an enhanced solar-like flare activity (see reviews by Montmerle et al. 1993; and Feigelson & Montmerle 1999, hereafter FM). Casanova et al. (1995) – hereafter CMFA – reported deep *ROSAT Position Sensitive Proportional Counter (PSPC)* imaging of the ρ Oph cloud dense cores A and F. They detected in the $35' \times 35'$ central portion of the field (the inner ring of the *ROSAT* detector entrance window support structure) 55 X-ray sources in the 1.0–2.4 keV energy band. For three X-ray sources, one or several Class I sources lie within the error boxes of X-ray peaks, but other counterparts are possible (unclassified IR sources, T Tauri stars). X-ray emission from one of these Class I sources, YLW15 (=IRS43 in WLY), was unambiguously confirmed with a follow-up *ROSAT High Resolution Imager (HRI)* observation by Grosso et al. (1997). The outer portion of the CMFA *PSPC* field, analyzed by Casanova (1994), contains 36 X-ray sources. The optical spectroscopic classification of these X-ray sources and other X-ray selected stars in the ρ Oph dark cloud vicinity, based on H_α and Li I (670.8 nm) spectroscopy, was made by Martín et al. (1998), doubling the number of PMS stars spectroscopically classified in the ρ Ophiuchi area.

Observations of harder X-ray (> 4 keV) from the ρ Oph dark cloud were initially only possible with non-imaging instruments. *Tenma* and *Ginga* revealed unresolved emission from the cloud core region, with a hard X-ray spectrum with $kT_X \sim 4$ keV and $N_H \sim 10^{22} \text{ cm}^{-2}$ (Koyama 1987; Koyama et al. 1992). Wide-energy band imaging observations became possible with *ASCA* in the range 0.5–10 keV. In the ρ Oph dark cloud, Koyama et al. (1994) detected hard X-rays from T Tauri stars, with kT_X up to ~ 8 keV in the case of the WTTS DoAr21. There is also some evidence for unresolved hard X-ray emission from embedded young stars below the point source detection limit. From this *ASCA* observation, Kamata et al. (1997), found additional T Tauri stars and detected three X-ray sources associated with Class I sources, but with large X-ray error boxes ($15'' - 30''$).

There is a deep connection between IR and X-ray observations of star-forming regions. Sensitive ground-based near-IR surveys penetrate dark clouds (except for dense cores) so that their source populations are frequently dom-

inated by ordinary stars in the Galactic disk. Space-based mid-IR isolates YSO with significant circumstellar material and effectively eliminates the background star population, but they will miss the recognition of YSO with less massive or absent disks. X-ray emission, in contrast, is elevated by 1–4 orders of magnitude in YSO of all ages, irrespective of a disk presence. It thus provides a unique tool for improving the census of young star clusters.

In this article, we present the results from the *HRI* follow-up of the CMFA *PSPC* observation. The high angular resolution of these observations allows us to find counterparts to all X-ray sources without ambiguity. The comparison with the sensitive *ISOCAM* survey of the ρ Oph dark cloud significantly improves the existing classification of these counterparts and allows us to do statistical studies on a well defined sample.

We first present the *ROSAT HRI* observations: image analysis, source detection and identification (§2). We incorporate the *ISOCAM* survey results from Bontemps et al. (2000) and we present the resulting IR classification for the *HRI* sources (§3). The next sections discuss the X-ray luminosity of the *HRI* detected TTS (§4), and the X-ray detectability of the embedded TTS population (§5). Next (§6), we show that the *HRI* census of Class III sources cannot be complete, and that numerous unknown low-luminosity Class III sources, perhaps including brown dwarfs, must exist. Summary of the main results and conclusions are presented in §7, where prospects for improvements with *XMM-Newton* and *Chandra*, are also discussed.

Appendix A gives details about the *HRI* X-ray source detection, and lists the X-ray detections. Optical finding charts, and identification list of the *HRI* X-ray sources can be found in Appendix B. Appendix C compares these *HRI* observations with previous *PSPC* ones. Appendix D discusses the status of optical/IR counterparts without IR classification.

2. The ROSAT HRI X-ray observations

2.1. The ROSAT HRI images

We have observed the dense cores A and F of the ρ Oph dark cloud with the *ROSAT HRI*. The detector is sensitive to the 0.1–2.4 keV energy range, but has no spectral resolution. The two observation fields were respectively centered on approximately the WTTS DoAr21 ($\alpha = 16^{\text{h}}26^{\text{m}}2^{\text{s}}.4$, $\delta = -24^{\circ}23'24''$ [J2000]) and on the Class I protostar YLW15 = IRS43 ($\alpha = 16^{\text{h}}27^{\text{m}}26^{\text{s}}.4$, $\delta = -24^{\circ}40'48''$ [J2000]). *ROSAT HRI* images have a diameter of $\sim 40'$. Fig. 1 displays the two observation fields, which include the dense DCO^+ cores A, B, C, E, and F (Loren et al. 1990), most of the area studied by CMFA and *ASCA*, as well as the *ISOCAM* survey. The first observation field, centered approximately on ρ Oph A, will be referred to as the “core A field”; the second observation

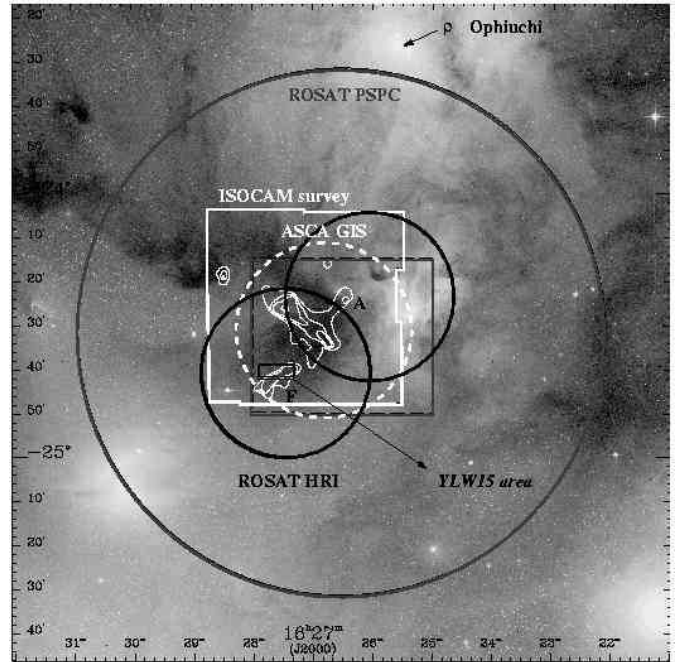


Fig. 1. Map of the ρ Ophiuchi dark cloud observation fields. 2° diameter *ROSAT PSPC* field of view, and its central $35' \times 35'$ studied by Casanova et al. (1995); $40'$ diameter *ROSAT HRI* fields of view and YLW15 area published in Grosso et al. (1997); *ASCA GIS* field of view from Koyama et al. (1994) and Kamata et al. (1997); *ISOCAM* survey field (central programme observations by Nordh et al.; see Abergel et al. 1996). The background image of the ρ Ophiuchi star forming region is taken from the first Digitized Sky Survey, contrast was enhanced with Gaussian histogram specification (Canzian 1997). Regions of high visual extinction are clearly visible. DCO^+ (J=2-1) contours from Loren et al. (1990) show for reference the location of dense cores A, F.

field, centered on dense core F, will be called the “core F field”. The core A field was observed between 1995 August 29 and 1995 September 12 with a total exposure of 51.3 ks. The core F field was observed at three different epochs (hereafter observations #1, #2, and #3): between 1995 March 9 and 14 (12.5 ks), between 1995 August 18 and 20 (27.5 ks), and between 1996 September 7 and 11 (37.2 ks). These three different epochs give a total exposure of 77.2 ks (see Table 1 for the log of *ROSAT HRI* observations details).

2.2. The HRI image analysis

We have analyzed separately the four data sets. Standard source detection algorithms were used to find X-ray sources, and to search optical counterparts for each set. We then selected X-ray sources with the best position accuracy (usually the brightest not too far away from the field center) and having an unambiguous counterpart,

Table 1. Log of *ROSAT HRI* Observations.

Pointing ID	Core	Obs. #	Begin		End		Elapsed Time [ks]	Exposure [ks]
			Date	Hour (UT)	Date	Hour (UT)		
201835h	A	1	1995 Aug 29	18 ^h 31 ^m 30 ^s	1995 Sep 12	22 ^h 35 ^m 47 ^s	1 224.3	51.3
201834h	F	1	1995 Mar 09	00 ^h 51 ^m 03 ^s	1995 Mar 14	05 ^h 16 ^m 43 ^s	447.9	12.5
201834h-1	F	2	1995 Aug 18	19 ^h 29 ^m 21 ^s	1995 Aug 20	14 ^h 52 ^m 05 ^s	27.8	27.5
201834h-2	F	3	1996 Sep 07	23 ^h 12 ^m 46 ^s	1996 Sep 11	13 ^h 46 ^m 23 ^s	311.6	37.2
	F	1+2+3	1995 Mar 09	00 ^h 51 ^m 03 ^s	1996 Sep 11	13 ^h 46 ^m 23 ^s	47 739.3	77.2

corrected all X-ray positions from the existing offsets, and used this improved astrometry to remove possible ambiguities in the identification of the X-ray sources. Details can be found in Appendix A.

We find 63 *HRI* X-ray sources. Fig. 2 shows the positions of these sources, superimposed on a combined IR and optical image of the ρ Oph cloud. Coordinates, error boxes, likelihoods of existence, and count rates of these *HRI* X-ray sources can be found in Appendix A (Table A.1).

2.3. *HRI* X-ray source identifications

Identification of the *HRI* X-ray sources was made by cross-correlations with published lists of confirmed or suspected cloud members (AM), IR surveys (Greene & Young 1992; BKLT; and Bontemps et al. 2000, see §3), *K*-band spectroscopic (Luhman & Rieke 1999), radio surveys (André, Montmerle, & Feigelson 1987; Stine et al. 1988; Leous et al. 1991), and with previously known X-ray sources (*PSPC*: CMFA, Martín et al. 1998; *ASCA*: Kamata et al. 1997). For X-ray sources without published counterparts we have used *SIMBAD*,¹ and we have also searched optical counterparts on optical red band images from the Digitized Sky Survey.²

As shown by the finding charts in Appendix B, thanks to the good angular resolution of the *ROSAT HRI* (PSF FWHM $\sim 5''$ on axis; due to the mirrors as well as the detector), the position accuracy ($1''$ – $6''$, see Col. 6 Table A.1) allows us to find counterparts almost without ambiguity.³ Identification lists for the core A and core F fields are given in Appendix B, Table B.1. We also discuss in Appendix B the identification of X-ray sources with a low statistical significance.

Nearly 90% of the *HRI* X-ray sources are identified. We detect only $\sim 70\%$ of the *PSPC* X-ray sources (CMFA;

Casanova 1994), but this can be explained by the difference in sensitivity between the two instruments, and the intrinsic variability of the X-ray sources (see Appendix C).

3. Nature and IR properties of the *HRI* sources

Following the results of CMFA, essentially all X-ray sources we found in the ρ Ophiuchi dark cloud should be young stars, a number of them being still embedded in the cloud. Embedded YSO are mainly studied at IR and millimeter wavelengths, but they may all be potential X-ray emitter regardless of their IR classification. Indeed, using the results of Wilking et al. (1989), AM, and GWAYL, CMFA analyzed their results in the light of the IR observations of the stars they observed in X-rays. We can then (i) use the published IR surveys to provide a list of recognized YSO members of the cluster to be compared to the observed X-ray properties, and (ii) use X-ray emission to discriminate between true cluster members and the many potential background stars seen in IR images.

3.1. New Class II and Class III source census after *ISOCAM*

Near-IR surveys of the ρ Ophiuchi cluster, sensitive enough to detect low-luminosity embedded young stars, have recently been published (Comerón et al. 1993; Strom et al. 1995 – hereafter SKS; BKLT). However these ground-based surveys encountered limitations in recognizing the nature of all the embedded sources, and have therefore not much increased the number of *bona fide* members of the ρ Oph cluster. The mid-IR camera aboard *ISO*, *ISOCAM*, produced a map of the ρ Oph main cloud, used by Bontemps et al. (2000) to study the young star population. This mid-IR study resulted in a significantly more complete census of the ρ Oph cluster population. We here use this new census as a basis for discussion about the nature of the detected X-ray sources and to estimate the occurrence and properties of the X-ray emission of the different classes of YSO.

The mid-IR photometry at 6.7 and 14.3 μm appears invaluable to characterize sources with IR excesses, i.e., Class I sources and Class II sources (e.g., Nordh et al. 1996; Bontemps et al. 1998). In ρ Oph, Bontemps et al. (2000) have doubled the number of Class II sources known.

¹ On-line version at <http://simbad.u-strasbg.fr/Simbad>.

² On-line version on the ESO site: <http://arch-http.hq.eso.org/cgi-bin/dss>.

³ When two possible counterparts are in the error box (this happens only three times, see the finding charts in Appendix B, and Table B.1 notes), we take the more luminous in the *J*-band, since the X-ray luminosity of TTS is correlated with the *J*-band luminosity (see CMFA, and below §3.2, §7.2).

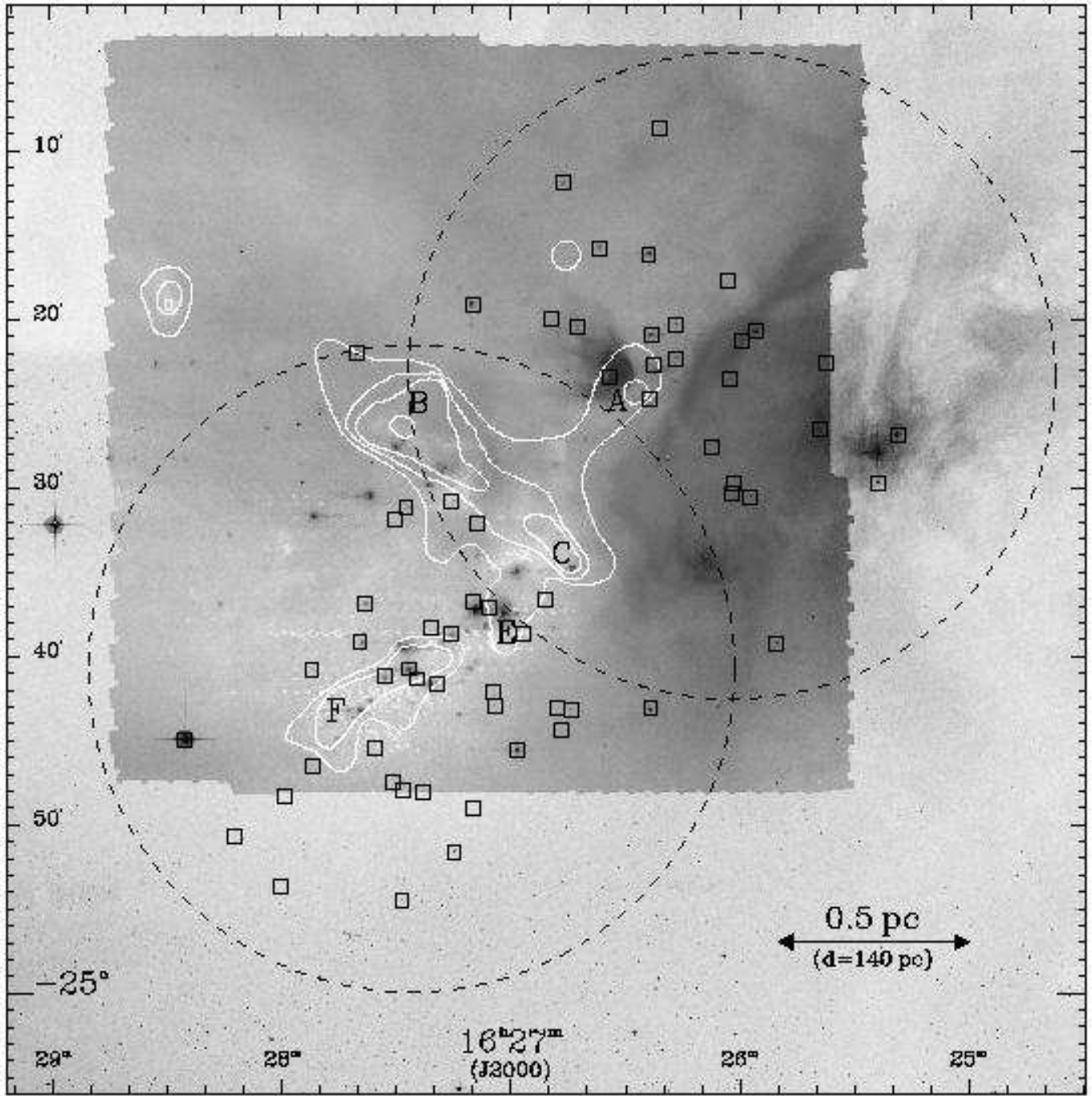


Fig. 2. X-ray sources in the *ROSAT HRI* fields. The composite *ISOCAM* map of Abergel et al. (1996) (LW2 filter image [5–8.5 μm], plus LW3 filter image [12–18 μm]) is merged with the background optical image taken from the first Digitized Sky Survey. DCO⁺(J=2-1) contours show the location of dense cores named A, B, C, E, F by Loren et al. (1990). A scale of 0.5 pc is shown for $d = 140$ pc. The positions of the X-ray sources are marked by 50''-size squares. Typical X-ray error positions range between 1''–6''.

These authors conclude that the sample is complete down to stellar luminosities, L_* , as low as $0.03 L_{\odot}$, thus extending downwards the luminosity function obtained from the ground by about one order of magnitude. However, just as in the near-IR, these measurements alone cannot characterize the nature of sources without IR excess: these can

be either Class III sources (diskless TTS) or background sources.

The tentative Class III classification of a number of sources coming from previous X-ray observation (CMFA), or from this article, is now confirmed by *ISOCAM*, which

detected no IR excess. We call these sources “new” Class III sources (see Table B.1, and §5).

Since we already identified one of the *HRI* sources as a foreground star (ROXF37 = HD148352, see Table B.1), the question arises that a number of these new sources with Class III spectra may also be field stars, contaminating the genuine young star sample. Guillout et al. (1996) has estimated the stellar content of flux-limited X-ray surveys, based on the age-dependent stellar population model developed by the Besançon group. For the average sensitivity of our *HRI* observation ($\sim 6 \times 10^{-4}$ cts s $^{-1}$, see Fig. 6), the ρ Oph galactic latitude ($\sim 20^\circ$), and our total field of view (0.5 square degrees), this model yields an estimate of 5 contaminating stars (P. Guillout, private communication). Removing HD148352, this leaves 4 possible field star candidates among the 21 “new” Class III sources and “Class II-III” sources listed in Table B.1. This number is small enough not to affect significantly our discussion, and in what follows we will simply neglect the possible contamination of our various Class III samples by field stars.

The Class III source population will be studied in detail below (§4 and §6).

3.2. Cloud extinctions and stellar luminosities from near-IR photometry

YSO suffer from large amounts of extinction by dust – cloud dust plus circumstellar dust – (up to $A_V = 60$ or more in ρ Oph), which strongly affects their fluxes at all wavelengths of interest, but does not necessarily prevent their detection in soft X-rays (see, e.g., CMFA). Despite this effect, it is possible to estimate the total extinctions along the line of sight and stellar luminosities. Near-IR photometry data appear to provide the most reliable estimate for the luminosity of the embedded young stars (see discussion in Bontemps et al. 2000 and references therein): the *J*-band fluxes are usually almost purely photospheric and thus trace the stellar luminosities very well (e.g., GWAYL; SKS). Similarly the *J* – *H* color is a sensitive tracer of interstellar extinction. We therefore use the extinctions and stellar luminosities derived from near-IR photometry for the ISOCAM sample by Bontemps et al. (2000).

In CMFA the bolometric luminosities were approximately estimated from the *J*-band fluxes using the GWAYL conversion based on an observational correlation between *J* fluxes and bolometric luminosities for Taurus and Chameleon TTS. The bolometric luminosity comprises in principle the total luminosity (accretion + stellar) of a YSO. However for young PMS stars like Class II sources and Class III sources, this luminosity should coincide with their stellar luminosity since their accretion luminosity (if any) has become significantly smaller than the photospheric luminosity. Finally we note that the conversion between the *J*-band absolute magnitude and the

stellar luminosity used by Bontemps et al. (2000) is numerically similar to the CMFA conversion between the dereddened *J*-band and the bolometric luminosity.

Cols. 8–9 of Table B.1 give for each source its more up-to-date values of interstellar extinction and stellar luminosity, determined by Bontemps et al for 140 pc. The reader will find the details of the calculations in Bontemps et al. (2000).

3.3. Nature of the HRI sources from IR data

The YSO evolutionary stage, inferred from IR spectral energy distributions (see §3.1), is available for most of the X-ray sources. The resulting census of the 55 X-ray sources with stellar counterparts is: one Class I protostar (YLW15=IRS43); 23 Class II sources, including 4 new ISOCAM Class II sources; 21 Class III sources, including 13 new Class III sources⁴; 8 whose classification is either Class II or Class III sources (see discussion in Appendix D); one Class III early-type star (S1, with spectral type B3; see André et al. 1988), and one main sequence foreground star (HD148352 with spectral type F2V; see the *Hipparcos* catalogue).

In Table B.1, Col. 6 lists cross-identifications with the ISOCAM survey: *red* (*blue*) means ISOCAM sources with (without) IR excess. Col. 7 gives the IR classification, Cols. 8–9 the extinctions and stellar luminosities (from Bontemps et al. 2000).

Therefore, the present analysis has revealed no new X-ray emitting Class I source, apart from the Class I protostar YLW15 which has been the subject of a specific study (Grosso et al. 1997). The *HRI/ISOCAM* sources are overwhelmingly TTS, for which improved results are described in the following sections.

4. X-ray luminosities of the HRI-detected T Tauri stars

4.1. Derivation from source count rates

We assume a fiducial TTS X-ray spectrum (see Montmerle 1996) having $kT_X=1$ keV plasma, with cosmic abundances, and Raymond-Smith line emissivities, and with interstellar absorption based on Morrison & McCammon (1983) cross sections. We use the relation given by Ryter (1996) to estimate the hydrogen column density, N_H , from the visual extinction, A_V , determined from IR data⁵: $N_H = 2.23 \times 10^{21} A_V \text{ cm}^{-2}$. The intrinsic (i.e., extinction corrected) X-ray luminosities in the full *ROSAT* en-

⁴ 4 were already *PSPC* Class III source candidates, and are confirmed by *ISOCAM*, which detected no IR excess; 3 were probably detected by the *PSPC*, but due to its lower angular resolution the optical or IR counterpart was uncertain (see Col. 2 of Table B.1 and attached notes); 6 are genuine new X-ray detections, probably resulting from variability.

⁵ Noted $A_{V,IR}$ in CMFA.

ergy band (0.1–2.4 keV), L_X , were calculated for classified sources from source count rates for $d \sim 140$ pc using EXSAS, and are given in Cols. 10–13 of Table B.1. The intrinsic X-ray luminosities span the range $L_X \sim 1 \times 10^{29} - \sim 4 \times 10^{31} \text{ erg s}^{-1}$. (For X-ray sources without extinction estimates we label the detection exposure with a question mark.)

4.2. Luminosity functions of HRI-detected Class II and Class III sources

We here compare the extinction corrected X-ray luminosities of the Class II and Class III sources detected by the *HRI* in the *ISOCAM* field⁶ in order to evaluate the contribution of the circumstellar disk to the X-ray absorption, or to the X-ray emission (for instance by magnetic reconnection between the star and the disk; see Montmerle et al. 2000).

Fig. 3 shows the cumulative X-ray luminosity distribution functions for these two populations, estimated using the ASURV statistical software package (rev. 1.2;⁷ La Valley et al. 1992), which takes upper limits into account. These distributions are mathematically identical to the maximum likelihood Kaplan-Meier estimator (Feigelson & Nelson 1985). Their mean X-ray luminosities (in erg s^{-1}) are given by $\langle \log(L_X) \rangle = 30.3 \pm 0.1$ for Class II sources, and $\langle \log(L_X) \rangle = 30.4 \pm 0.2$ for Class III sources. We used nonparametric two-sample tests implemented in ASURV — Gehan’s generalized Wilcoxon test, Logrank test, Peto & Peto generalized Wilcoxon test, Peto & Prentice generalized Wilcoxon test — to see whether the difference between the two luminosity functions is significant. These tests gave a high probability (46–72 %) that they are statistically indistinguishable. This result agrees with previous deep studies of the ρ Oph main cloud (CMFA) and Chamaeleon I (Feigelson et al. 1993; Lawson et al. 1996) YSO populations.

In contrast, Neuhäuser et al. (1995) found in the Taurus-Auriga star-forming region that Class III sources are more X-ray luminous than Class II sources. Neuhäuser et al. (1995) used the *ROSAT All Sky Survey (RASS)* to cover a large area of the Taurus-Auriga (~ 900 square degrees), including dense cores, but also away from this star-forming region. This shallow survey and large area must be compared to our deep pointed observations, where our field of interest covers 0.5 square degrees. In our observations we focus only on the dense cores, studying a younger population of YSO. Contamination of the T Tauri star sample by a more evolved, wide-spread, and older Class III

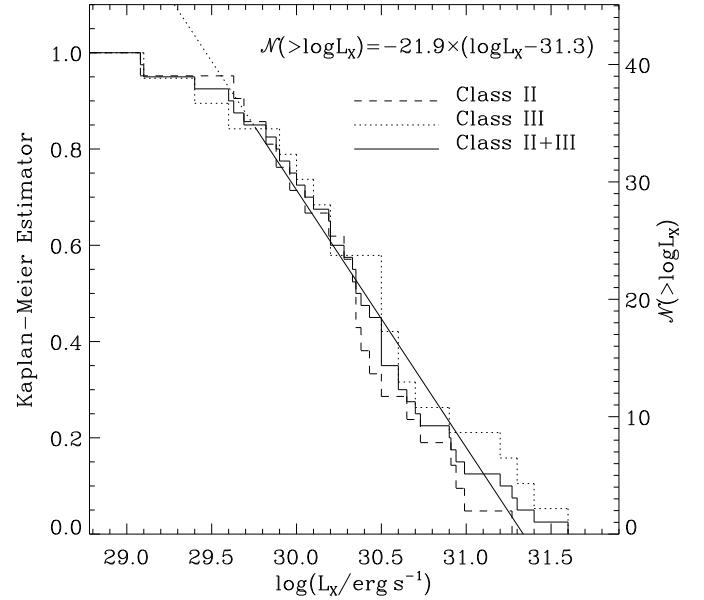


Fig. 3. Cumulative normalized X-ray luminosity functions of Class II and Class III sources detected with the *HRI* in the ρ Oph cloud. The dashed (dotted) histogram shows the Class II (Class III) source integral X-ray luminosity functions. The solid histogram shows the total cumulative X-ray luminosity functions. The straight line shows the fit for the total cumulative X-ray luminosity functions. The left scale gives the Kaplan-Meier estimator. The right scale gives the cumulative number of X-ray sources.

source population, may explain the discrepancy with the result of Neuhäuser et al. (1995).⁸

Thus, we confirm that the contribution of the disk of Class II sources to their X-ray emission, or to X-ray absorption, must be small.

Next, we combine the X-ray luminosity distributions of Class II and Class III sources to obtain the cumulative X-ray luminosity distribution function of all TTS detected by the *HRI*. For $\log(L_X)$ between 29.7 ($\log(L_{X,\text{break}})$) and 31.3 ($\log(L_{X,\text{max}})$), the distribution is loglinear: $\mathcal{N}(>\log(L_X)) = -21.9 \times (\log(L_X) - 31.3)$. For $\log(L_X) \leq \log(L_{X,\text{break}})$, the distribution shows a downwards trend, which is due to our lower efficiency to detect weak X-ray emitting TTS. We deduce from this linear relation the total X-ray luminosity emitted by the X-ray sources with X-ray luminosity between $L_{X,\text{max}}$ and $L_{X,\text{min}}$ (an arbitrary value): $L_{X,\text{tot}} = 21.9 \times (L_{X,\text{max}} - L_{X,\text{min}})$. Thus, the total X-ray luminosity of this group of X-ray sources is dominated by the brightest sources (with $L_{X,\text{max}}$), and is very weakly dependent on the loglinear fit. For $L_{X,\text{min}} = L_{X,\text{break}}$, we find $L_{X,\text{tot}} \sim 4.3 \times 10^{32} \text{ erg s}^{-1}$. This value is close to the asymptotic value $4.4 \times 10^{32} \text{ erg s}^{-1}$ obtained

⁶ 22 Class II sources and 19 Class III sources; for the core F observation we take the mean X-ray luminosity in Col. 13 of Table B.1.

⁷ Version available at <http://www.astro.psu.edu/statcodes>.

⁸ In addition one should note that the *RASS* includes the soft band (0.1–1 keV), which is more sensitive to the extinction than the hard band (1–2.4 keV) taken by CMFA.

taking $L_{X,\min} = 0$, thus future detections of new X-ray emitting TTS with low X-ray luminosity will not greatly affect this result.

4.3. HRI source variability

We present in Appendix C a study of the variability of the X-ray sources which were observed both by the *HRI* and the *PSPC*, and we show that some sources were in a high X-ray state during the *HRI* or the *PSPC* observations. Here, we study the variability of the Core F *HRI* sources.

Core F observations comprise three time-separated observations, which allow us to reiterate the ‘‘Christmas tree’’ luminosity study made with *Einstein Observatory* by Montmerle et al. (1983). The idea suggested by the similarity between Class II sources and Class III sources in X-rays was to assume that all the X-ray sources are basically one single type of X-ray object, seen in different states. The result was that the distribution of the flux variations could be approximated by a power-law with an index $\beta = -1.4$.

We have estimated whenever possible for each Core F *HRI* source the X-ray flux variations from the observed high/low luminosity ratio, $\mathcal{R} \equiv L_{X,\text{high}}/L_{X,\text{low}}$, based on the three observations. This yields 27 values including 11

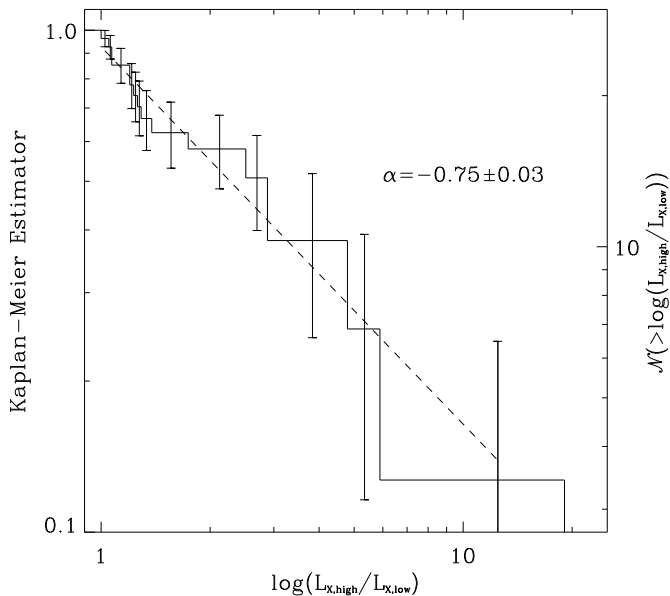


Fig. 4. Distribution of X-ray luminosity variations. We have estimated whenever possible for each X-ray source of core F the X-ray variability amplitude with the ratio high-on low-observed luminosity during the three observations. The frequency distribution has been estimated using the maximum likelihood Kaplan-Meier estimator. We find a power-law distribution: $\mathcal{N}(> \frac{L_{X,\text{high}}}{L_{X,\text{low}}}) \propto (\frac{L_{X,\text{high}}}{L_{X,\text{low}}})^\alpha$, with $\alpha = -0.75 \pm 0.03$, consistent with a variability due to stellar flares, which supports the analogy with the solar magnetic activity.

lower limits. The integral distribution for a given ratio is estimated using the maximum likelihood Kaplan-Meier estimator (see Fig. 4). We find a power-law distribution: $\mathcal{N}(> L_{X,\text{high}}/L_{X,\text{low}}) \propto (L_{X,\text{high}}/L_{X,\text{low}})^\alpha$, with an index $\alpha = -0.75 \pm 0.03$. This implies that the differential distribution $d\mathcal{N}/d\mathcal{R}$ follows a power-law distribution of slope $\beta = \alpha - 1 = -1.75$.

We suggest following Montmerle et al. (1983) that this power-law behavior, may be explained in terms of variability due to stellar flares, if interpreted in terms of stochastic relaxation phenomenon (Rosner & Vaiana 1978), and dominating the X-ray activity of the underlying stars. Such a power-law behavior is seen in the solar flares in radio, optical, soft and hard X-ray emission with the power-law index $-\beta=1.1-3.0$ (see review in Aschwanden et al. 1998). For soft X-ray emission $-\beta=1.7-1.9$, which is consistent with our result, and supports the analogy with the solar magnetic activity.

5. X-ray detectability of the embedded T Tauri star population

We use the information given both by the *ISOCAM* survey and by our *HRI* deep exposure to study the X-ray detected TTS population of the ρ Oph dense cores. We restrict the following studies to the *HRI/ISOCAM* overlapping area.⁹ This area comprises 98 Class II sources (classified from ground-based and *ISO* observations), including 52 new *ISOCAM* Class II sources,¹⁰ and 35 Class III sources (characterized as YSO from X-ray or radio observations, and classified as Class III sources from ground-based and *ISO* observations), including 21 new Class III sources (*HRI* or *PSPC* X-ray sources without IR excess observed by *ISOCAM*). We will call these sources the ‘‘TTS sample’’.

Our *HRI* observation detected a large number of sources, yet these constitute only 30% of the ‘‘TTS sample’’. In this section, we examine the reasons why the other TTS were not detected, and in particular whether the undetected TTS form a separate population of genuinely X-ray weak objects.

5.1. X-ray vs. stellar luminosities

First, to know more about the X-ray properties of the members of the whole TTS sample (with upper limits if they are not detected with the *HRI*), we examine whether a correlation exists between the X-ray luminosity and the

⁹ We took 19.2’ for the *HRI* field radius, because one of our sources (ROXRF31=SR9), is detected up to this angle from the axis in the Core F field.

¹⁰ We have excluded three new *ISOCAM* Class II sources for which we have only the *K* magnitude, and thus no A_V estimate. L_\star for these sources must be small, and/or A_V high, which implies a high upper limit on the intrinsic L_X . This does not affect the statistical results.

stellar luminosity (both corrected from extinction), and if so, whether it is the same as the one found in ρ Oph by CMFA. We chose for each Core F X-ray source its lowest X-ray luminosity (including *HRI* upper limits) to minimize the effects of X-ray variability. For TTS undetected by the *HRI*, we estimate count rate upper limits (3.25σ)¹¹

To establish the existence of a linear correlation between $\log L_X$ and $\log L_*$, we performed three statistical tests using ASURV: Cox’s proportional hazard model, the generalized Kendall τ test, and Spearman’s ρ test. The probability of the null hypothesis (i.e. that this correlation is not present) is $< 10^{-4}$ for each of the three tests. Thus, a strong linear correlation between $\log L_X$ and $\log L_*$ is indeed present. We found the linear regression coefficients by using the Estimation Maximization (EM) algorithm under Gaussian assumptions and the Buckley-James method. The Buckley-James method gave results similar to those of the EM algorithm, but with a larger uncertainty on the slope. As the Buckley-James method is semi-nonparametric, this suggests that the residuals of the linear correlation may be non-Gaussian. We thus conservatively keep the slope uncertainty given by the Buckley-James method. The L_X-L_* correlation is then given by (see Fig.5): $\log(L_X/\text{ergs}^{-1}) = (1.0 \pm 0.2) \times \log(L_*/L_\odot) + 30.1$. We note that the censoring fraction is so high that the correlation line misses most of the data points and depends entirely on the location of the few lowest detections. The correlation dispersion may be due to X-ray variability, and also to TTS spectral type and age differences: Neuhäuser et al. (1995) points out that the ratio L_X/L_* increases with decreasing effective temperature, and shows a variation of L_X with age.

This correlation spans three orders of magnitude in L_X and two in L_* . The slope of this correlation, a , is equal to 1.0, and the TTS X-ray luminosity is then approximately given by the simple proportionality: $L_X/L_* \sim 10^{-4}$. We thus confirm that the characteristic for TTS in ρ Oph is 10^{-4} , with a large dispersion up to a level $\sim 10^{-3}$. There is no evidence for the “saturation” effect seen at this level in late type main sequence stars, and attributed to the complete filling of the stellar surface by active regions (Fleming et al. 1989).

A similar correlation between L_X and L_* was found for Class II and Class III sources in the previous ρ Oph study of CMFA (the method used to estimate L_* was different, but very similar numerically; see §3.2), but also in other star-forming regions: Chamaeleon (Feigelson et al. 1993; Lawson et al. 1996), Taurus-Auriga (Neuhäuser et al. 1995), and IC 348 (Preibisch et al. 1996). However, the slopes may not be identical: while Feigelson et al. (1993),

¹¹ When the YSO is in both Core A and Core F field, we use the longer Core F field exposure to estimate the count rate upper limit. using the EXSAS command COMPUTE/UPPER_LIMITS, and we use the extinction estimate from Bontemps et al. (2000) to compute the corresponding limit on the intrinsic X-ray luminosity.

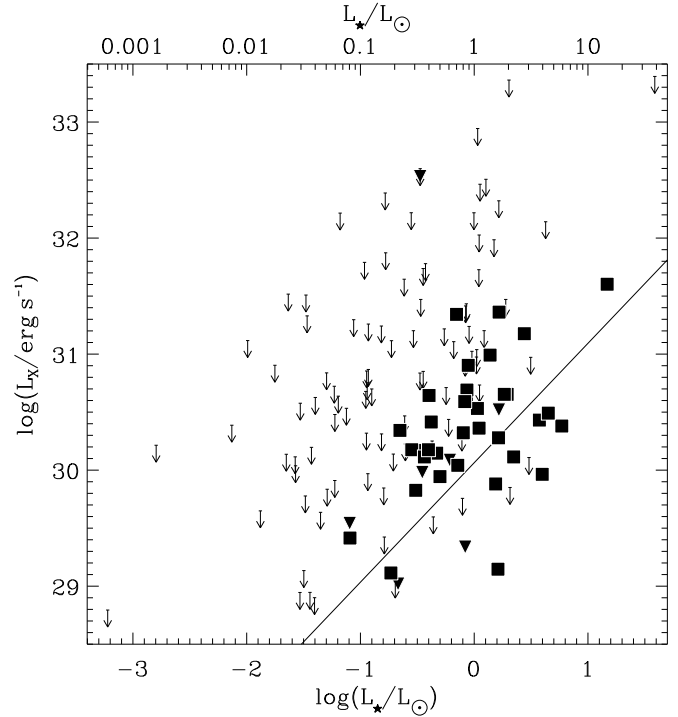


Fig. 5. Intrinsic X-ray and stellar luminosity correlation for the “T Tauri star sample”. The squares represent the T Tauri stars detected with the *HRI* in Core A observation, and the T Tauri stars detected with the *HRI* in Core F observations for which the lowest X-ray luminosity of the 3 observations is not an upper limit. Downward triangles correspond to the T Tauri stars detected with the *HRI* in Core F observations for which the lowest X-ray luminosity of the 3 observations is an upper limit. Arrows are the hundred upper limits for the *HRI* undetected T Tauri stars. The highest upper limits correspond to high extinction sources (see Fig. 7). The solid line shows the correlation found using ASURV: $\log(L_X/\text{ergs}^{-1}) = (1.0 \pm 0.2) \times \log(L_*/L_\odot) + 30.1$.

Preibisch et al. (1996), and CMFA find the same $a = 1$ slope as above. On the other hand, Lawson et al. (1996) found $a = 0.55$, on a better characterized, enlarged X-ray source sample in Chamaeleon, stressing the importance of having a sample as complete as possible. Nevertheless, the fact that we find the same slope as CMFA with an enlarged sample of X-ray sources in the same cloud is certainly a good internal consistency check between the *PSPC* and the *HRI*.

We find that the majority of the X-ray luminosity upper limits are above the L_X-L_* correlation. Only 5% of the X-ray undetected TTS are below the correlation, mixed with X-ray detected TTS. This is consistent with the idea that *all* TTS in ρ Oph may be X-ray emitters with $L_X/L_* \sim 10^{-4}$. Therefore, the TTS undetected by the *HRI* do not make up a separate population, but must

have X-ray properties comparable to that of the detected population, verifying the same correlation.

5.2. The X-ray undetected T Tauri star population

Using the previous correlation between the stellar and X-ray luminosities, we can now estimate for each member of the TTS sample the intrinsic X-ray luminosity in the *ROSAT* energy band,¹² and compare it with the *HRI* detection threshold to understand the X-ray detectability of the TTS sample with the *HRI*. However, the comparison is not straightforward, since the *HRI* detection threshold depends on both instrumental effects and extinction along the line of sight.

Fig. 6 shows the instrumental effects: the *HRI* count rate threshold (3.25σ) increases away from the pointing axis. We interpret this dependence as the consequence of the point spread function degradation and reduced sensitivity off-axis of the *ROSAT* mirrors (David et al. 1997). With the X-ray spectrum assumptions described in §4.1, we have determined using EXSAS the conversion factor, f , between the *HRI* counts and the apparent X-ray luminosity (i.e., in the absence of extinction) in the *ROSAT* energy band (0.1–2.4 keV), $L_{X,app}$. We find: $f = 6.8 \times 10^{28} \text{ erg cts}^{-1} \text{ s}$ for $d = 140 \text{ pc}$. The minimum X-ray luminosity for a 3.25σ *HRI* detection, $L_{X,min}$, ranges from $\sim 7 \times 10^{27} \text{ erg s}^{-1}$ on-axis (angle=0') to $\sim 7 \times 10^{28} \text{ erg s}^{-1}$ off-axis (angle=19.2') (see Fig. 6).

In case the X-ray sources suffer some extinction equivalent to A_V magnitudes, the values of $L_{X,min}$ on-axis and off-axis must be corrected to obtain the corresponding *intrinsic* minimum X-ray luminosities as a function of A_V : if a source is heavily extinguished, this minimum may be up to two orders of magnitude higher or more than in the absence of extinction (see for example the high values of the upper limits of Fig. 5).

Fig. 7 plots the X-ray luminosities of the TTS sample as a function of A_V (or N_H). These X-ray luminosities were estimated from the stellar luminosities using the correlation discussed in the previous section. The points are compared with the *HRI* threshold curves $L_{X,min} = f(A_V)$, computed both on-axis and off-axis. The *HRI* detected TTS (crossed dots) are found to be rather bright ($\sim 10^{29} - \sim 10^{31} \text{ erg s}^{-1}$) and weakly extinguished ($A_V \leq 10$). The undetected TTS have estimated X-ray luminosities below the computed *HRI* detection threshold. In particular, we understand why the new *ISOCAM* Class II sources (Bontemps et al. 2000), characterized both by low stellar luminosities ($\sim 0.05 L_\odot$) (and thus presumably low predicted X-ray luminosities, $\sim 6 \times 10^{28} \text{ erg s}^{-1}$), and rela-

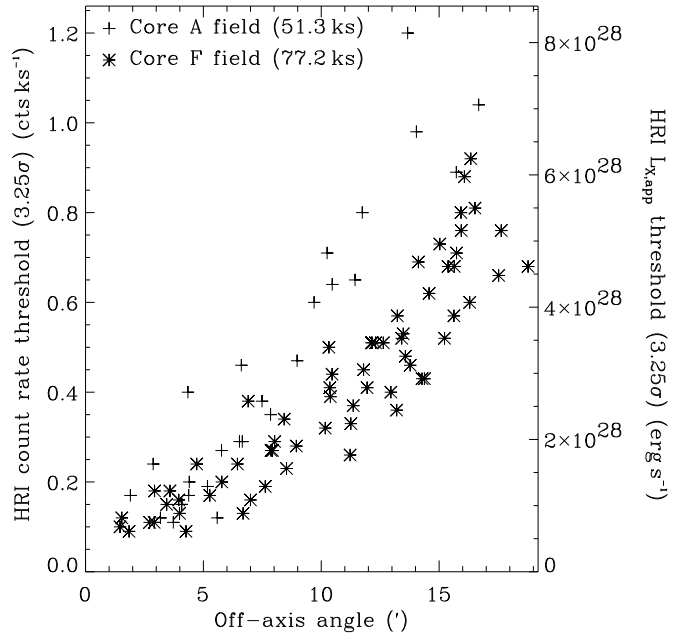


Fig. 6. *HRI* count rate thresholds (3.25σ) vs. off-axis distance (*bottom scale*). *Left (resp. right) scale*: *HRI* count rate (resp. apparent X-ray luminosity) threshold (3.25σ). Plus signs (asterisks) represent Core A (F) T Tauri stars of the “T Tauri star sample” undetected with the *HRI*.

tively high extinctions ($A_V \sim 20$), could not have been detected with our *HRI* observation.¹³

Now *ISOCAM* cannot *per se* recognize Class III YSO among its sources without IR excess, but X-rays can. However, a reliable census of Class III sources in ρ Oph is *de facto* limited by the sensitivity of X-ray observations: Fig. 7 shows that the number of detected Class III sources decreases for low L_X and high A_V ; roughly speaking Class III sources are mainly detected above $L_{X,min} \sim 10^{29.6} \text{ erg s}^{-1}$ (or equivalently $L_{*,min} = 0.35 L_\odot$), and below $A_{V,min} \sim 30$.

This strongly suggests that unknown Class III sources may exist. We can estimate their number at least in regions at the periphery of cloud cores, by using the fact that the WTTS/CTTS ratio (or equivalently the Class III/Class II source ratio) is ~ 1 , and also that the *HRI* is equally sensitive to Class III and Class II sources (see §4). In the *HRI/ISOCAM* overlapping area, this ratio is $19/22 \sim 1$; on a comparable area Martín et al. (1998) also found a WTTS/CTTS ratio ~ 1 . Since the “TTS sample” comprises 88 Class II sources and 35 Class III sources above $L_* \sim 0.03 L_\odot$, we predict that

¹² We note that this method attributes a larger X-ray luminosity to the TTS having X-ray luminosities below the $L_X - L_*$ correlation. By this effect X-ray undetected TTS can be put above the *HRI* detection threshold, but this concerns only 5 cases, see Fig. 6.

¹³ A few faint sources were however detected in spite of being below the nominal *HRI* detection threshold: they were probably in an X-ray flaring state at the time of the observations. In particular ROXRF32 = GY238, far below the *HRI* detection threshold, was detected only in the third Core F exposure, which supports this interpretation.

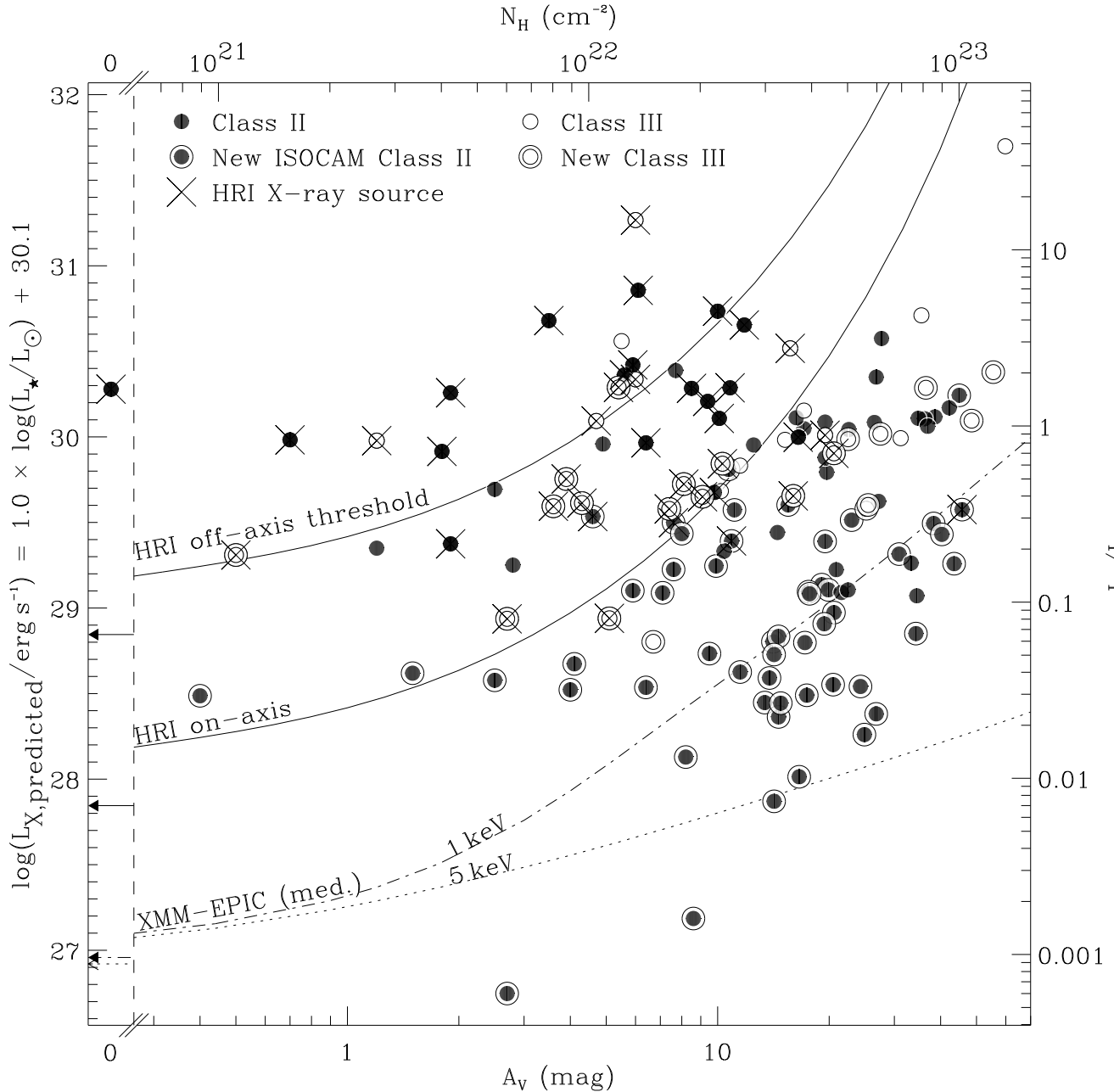


Fig. 7. Detectability of the “T Tauri star sample” with the *HRI* vs. extinction. *Right scale:* stellar luminosity determined from near-IR photometry; *left scale:* X-ray intrinsic luminosity predicted from the L_X - L_* correlation (see Fig. 5); *top scale:* extinction expressed in N_H ; *bottom scale:* extinction expressed in A_V . “New” *ISOCAM* Class II sources are IR sources with IR excess discovered by *ISOCAM*. “New” Class III sources are IR sources characterized as YSO candidates from X-ray or radio observations, and for which *ISOCAM* observed no IR excess. Crosses indicate T Tauri stars detected with the *HRI*. Solid curves show the detection threshold for the *ROSAT HRI* (on- and off-axis), assuming a Raymond-Smith spectrum with $kT_X=1$ keV and an exposure time of 77 182 s. Several T Tauri stars were detected despite being below the nominal *HRI* detection threshold: these sources have likely been detected in a flaring state (see text for details). Dashed-dotted curves show the *XMM-EPIC* (medium filter) detection threshold for the same spectrum and exposure time; we assumed a noise of 4×10^{-4} cts s^{-1} for the *EPIC-pn*, and deduced the detection threshold for the all *EPIC* instrument applying a 0.75 factor (see the *XMM* Users’ Handbook; Dahlem et al. 1999). The dotted curves show the *XMM-EPIC* (medium filter) detection threshold for an high plasma temperature of 5 keV (flare). The X-ray detection of the “T Tauri star sample” is limited by the *HRI* sensitivity. *XMM-EPIC* thanks to its increased sensitivity and its energy range (0.2–12 keV), is less sensitive to extinction, and should be able to detect numerous new Class III sources, as well as the low-luminosity Class II sources discovered by *ISOCAM* (see text for details).

$(88 \times 19/22) - 35 \sim 40$ Class III sources remain to be discovered in X-rays in the *HRI/ISOCAM* overlapping area above $L_X \sim 3 \times 10^{28}$ ergs $^{-1}$. These sources are not seen now either (i) because they are too faint in X-rays ($L_X \leq L_{X,\min}$) –or equivalently from the existence of an L_X vs. L_* proportionality, too faint in stellar luminosity ($L_* \leq L_{*,\min}$)– or (ii) too absorbed ($A_V \geq A_{V,\min}$), or a combination of both. *XMM-Newton* will be an ideal tool to reveal such a large number of unknown Class III sources in the future (see §7), but, as shown in the next section, we can already figure out their nature to a large extent.

6. The unknown Class III source population

In this section, we seek to characterize the suspected unknown Class III source population, which is likely to exist on the basis of the Class II source findings by *ISOCAM* and other IR observations. We will use (i) the spatial distribution of all known Class II sources, and (ii) the extinction map derived from $C^{18}O$ observations.

6.1. Compared spatial distributions of the Class II and Class III sources

The conventional wisdom is that Class III sources are descendants of Class II sources after dispersion of their disks (e.g., Lada 1987; AM). As cloud cores have an internal velocity dispersion, stars form with an initial mean velocity distribution, implying that they drift away from their formation site (e.g., Feigelson 1996). This is the usual explanation for the increase with distance from cloud cores of the Class III/Class II source ratio (or equivalently at that stage the WTTS/CTTS ratio), which is $\lesssim 1$ within the core region (e.g., CMFA), and reaches values $\gg 1$ far from the cores (e.g., Martín et al. 1998). This implies a larger spread of the spatial distribution of the Class III source population compared to that of the Class II source population.

Let us first study the spatial distribution of the Class II source population within the *HRI/ISOCAM* area. We analyze the source surface density by using a 2-D Gaussian filter of a given FWHM on source position. The choice of the FWHM is optimized to enhance the contrast between regions of low and high source density, and thus reveal any clustering. Fig. 8 shows the resulting density map, in the form of dashed contours obtained with FWHM=6'. The Class II sources show three strong density peaks well centered on DCO^+ cores A, B and F, which is consistent with the idea that most of these sources were born in these cores. However, in spite of its comparable DCO^+ line-of-sight density, core C appears much poorer in Class II sources; the weaker star-forming activity of this core is confirmed by the presence of only one Class I source (see Bontemps et al. 2000).

One can go one step further by comparing the source distribution with the matter distribution along the line-

of-sight, i.e., with the extinction map. The DCO^+ radical is a good indicator of large densities ($n \sim 10^5\text{--}10^7$ cm $^{-3}$) in cold cores, but the relevant regions occupy a relatively small volume; by contrast, $C^{18}O$, which is generally optically thin and sensitive to smaller densities, is a good column-density tracer. Using this molecule, Wilking & Lada (1983) derived an extinction map of the ρ Oph cloud center, showing that the denser regions have an equivalent visual extinction A_V between ~ 30 and ~ 100 .

Fig. 8 displays the $C^{18}O$ contours, labeled in A_V by steps of $A_V \approx 20$, starting at $A_V = 36$, from Wilking & Lada (1983). Correspondingly, the Class II sources are represented by black dots of size decreasing with A_V , from low extinctions ($A_V < 9$) to high extinctions ($A_V \geq 45$), by steps of $A_V \approx 10$. A large majority of these sources are seen to have moderate extinctions ($A_V < 18$), even in the areas overlapping regions of high extinctions traced by $C^{18}O$. This implies that such sources are actually only moderately embedded in the cloud, *in front* of the densest regions traced by $C^{18}O$ and DCO^+ , rather than within them. The spatial distribution of the Class II sources can thus be more appropriately described as gaussian-like three-dimensional overlapping “haloes” around the DCO^+ cores A, B and F. This also implies that at least a fraction of the Class II sources with high extinctions are not necessarily really embedded in the densest regions, but may be part of these haloes *behind* the dense cores.

In the very same fashion, Fig. 9 displays the distribution of the known Class III sources, this time using FWHM=8'.¹⁴ This distribution is different from that of Class II sources in Fig 8. With respect to the DCO^+ cores, there is a strong density peak $\sim 5'$ SW of the location of core F, and no peak associated with cores A and B: in contrast with the distribution of Class II sources, there is a deficiency of Class III sources in the cloud center regions with high extinction.

The explanation for this apparent absence may be as follows. Whether they lie on the line-of-sight to regions of moderate extinction, or of high extinction, moderate-extinction Class II sources are found essentially everywhere. Therefore *we also expect to have low-extinction Class III sources everywhere*, in a $\sim 1:1$ proportion. If they are not detected with the *HRI*, it can thus only mean that they are too faint in X-rays, hence have a small stellar luminosity. In addition, as for Class II sources, we must expect along the line-of-sight to the densest regions of the cloud to also have moderately embedded Class III sources at the back of the cloud. Their spatial density should be roughly comparable to that of the unseen Class III sources in the front, i.e., yield a small absolute number given the compact size of the $C^{18}O$ cores.

¹⁴ A larger FWHM must be used because there are fewer Class III sources than Class II sources and because they are less clustered.

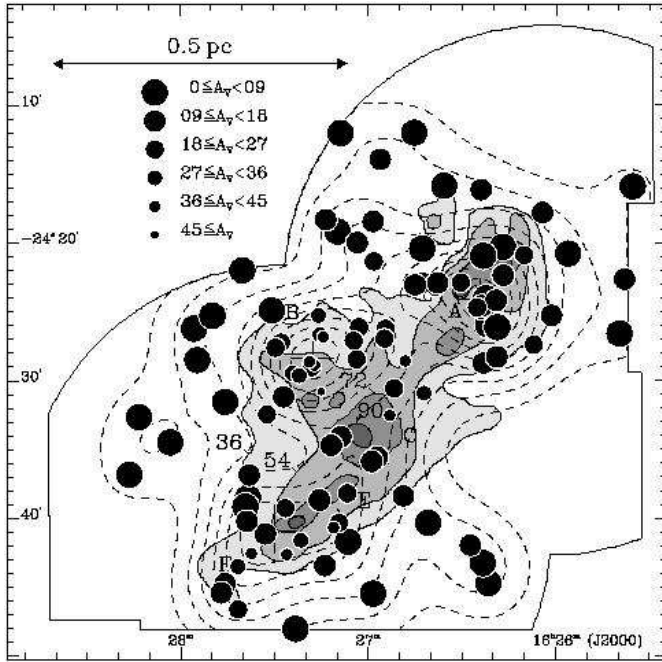


Fig. 8. Spatial distribution of Class II sources in the ρ Ophiuchi Cloud. Black dots show the position of Class II sources. The dot size gives information on the source visual extinction. The dashed contour map is an estimate of the local Class II source surface density (in linear arbitrary units) obtained using a sum of Gaussians (FWHM=6') centered on each Class II source position; crosses show the maxima of these peaks. The letters show the location of DCO⁺ (J=2-1) dense cores A, B, C, E, F (see Fig. 2). The contour map shows the visual extinction ($A_V=36, 54, 72, 90$) derived from C¹⁸O column density (Wilking & Lada 1983). A scale of 0.5 pc is shown for $d = 140$ pc.

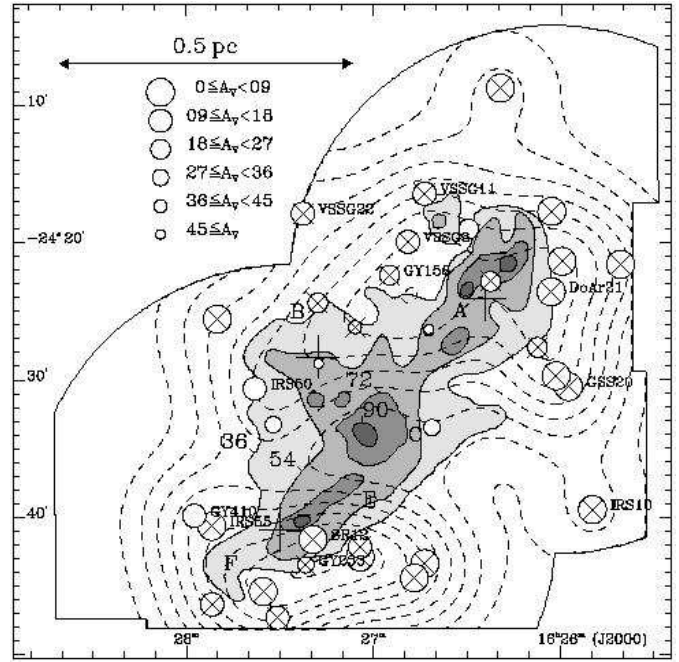


Fig. 9. Spatial distribution of Class III sources in the ρ Ophiuchi Cloud. White dots show the position of Class III sources excluding the early-type star S1. Crosses show X-ray detected Class III sources (Montmerle et al. 1983; CMFA; Koyama et al. 1994; Kamata et al. 1997; this article). The dashed contour map is an estimate of the Class III source surface density (in arbitrary linear units) obtained using a sum of Gaussians (FWHM=8') centered on each Class III source position. Plus signs show the positions of the density peaks of Class II sources (see Fig. 8). Class III sources with known spectral types are labeled, and put in an H-R diagram in Fig. 10.

There is also the possibility of having genuinely embedded (hence very young) Class III sources in these cores: we have no information about the Class III/Class II source ratio there, so it is impossible to estimate their number. Should this number be large (such that Class III/Class II > 1 for instance), this would be a problem for the earliest stages of YSO evolution; one rather expects to have Class III/Class II $\ll 1$ if all stars form with a disk taking at least $\gtrsim 10^5$ yr to dissipate. However, a disk stage is perhaps not necessary for very low-mass stars, which would increase the number of very young Class III sources.

6.2. Constraints on the nature of the unknown Class III sources

Let us construct the H-R diagram of the 12 Class III sources in *HRI/ISOCAM* area for which we know the spectral types from the optical observations of Bouvier & Appenzeller (1992), and from the *K*-band observations of Luhman & Rieke (1999), using the stellar luminosities

determined by Bontemps et al. (2000).¹⁵ Fig. 10 displays the result, along with the birthline and pre-main sequence evolutionary tracks of Palla & Stahler (1999). According to these evolutionary tracks, the ages of the 12 Class III sources are found to be spread between ~ 0.2 and ~ 5 Myr.

It is reasonable to assume that the unknown Class III sources have the same age spread. These sources are not yet detected in X-rays either because their intrinsic X-ray luminosities are too low, and/or because they have high extinctions. In the first case they have stellar luminosities below $0.35 L_\odot$, and the isochrones imply that $M_\star \sim 0.6 M_\odot$ for the oldest ones, and $M_\star < 0.1 M_\odot$ for the youngest ones. In the second case, however, the unknown embedded Class III sources can have luminosities higher than $L_{\star, \text{min}}$, i.e., so that they are not necessarily very low-mass stars.

Unless the number of Class III sources embedded in the densest regions is very high, our conclusion is that *the*

¹⁵ The relative differences between these luminosities, and the bolometric corrected ones from spectral types are lower than 20%.

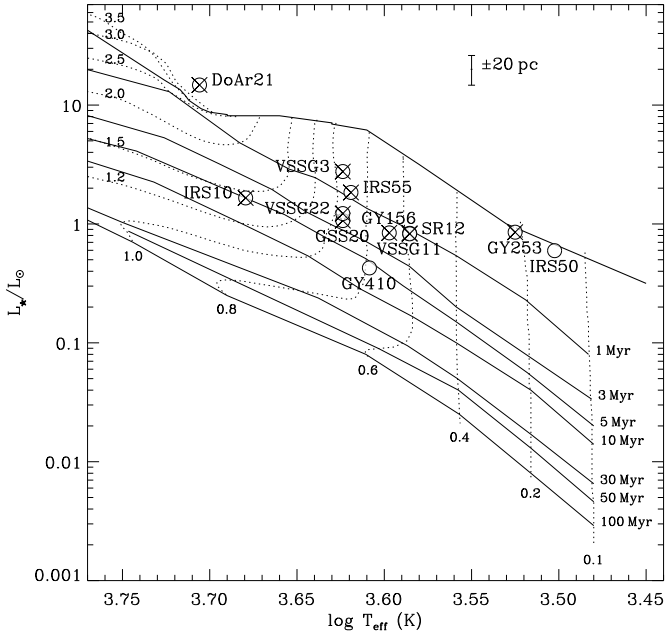


Fig. 10. H-R diagram for the Class III source with a known spectral types. Dotted lines show Palla & Stahler (1999) pre-main sequence tracks, continuous lines show isochrones. The bold continuous line represents the birth-line for the star build-up accretion rate ($10^{-5} M_{\odot} \text{ yr}^{-1}$). White dots show the position of Class III sources with known spectral type (Bouvier & Appenzeller 1992; Luhman & Rieke 1999; see also Greene & Meyer 1995), and using the Bontemps et al. (2000) luminosities. Crosses show X-ray detected Class III sources (Montmerle et al. 1983; CMFA; Koyama et al. 1994; Kamata et al. 1997; this article). We take $d = 140$ pc. The error bar shows the systematic luminosity error corresponding to a distance error of ± 20 pc.

bulk of the Class III sources which are undetected by the HRI and unrecognized by ISOCAM should be made of very low-mass stars.

7. Summary and conclusions

7.1. Main observational results

We have obtained two deep exposures of the ρ Oph cloud core region ($d=140$ pc) with the *ROSAT High Resolution Imager* (core A: 51 ks, core F: 77 ks, in three partial exposures). The improved position accuracy ($1''$ – $6''$) with respect to previous recent X-ray observations (*ROSAT PSPC*, Casanova et al. 1995; and *ASCA*, Koyama et al. 1994 and Kamata et al. 1997) have allowed us to remove a number of positional ambiguities for the detected sources. We have cross-correlated the X-ray positions with IR sources found in the *ISOCAM* survey of the same region at 6.7 and $14.3 \mu\text{m}$, in addition to sources known in the optical, IR, and radio from ground-based observations.

We thus have now at our disposal the best-studied sample of X-ray emitting YSO in a star-forming region. We first summarize the main observational results of this article.

- (1) We detect 63 *HRI* X-ray sources, and 55 are identified. Of the 55 identified X-ray sources 40 are *PSPC* sources, and 9 are *ASCA* sources.
- (2) The IR classification (ground-based and *ISOCAM* survey) for the 55 identified X-ray sources yields: one Class I protostar (YLW15=IRS43); 23 Class II sources, including 4 new *ISOCAM* Class II sources; 21 Class III sources, including 13 new Class III sources; 8 new Class II or Class III source candidates; one early-type Class III source (the young magnetic B3 star S1), and one field star (the F2V star HD148352). The contamination of the sample of new X-ray sources by field stars is negligible.
- (3) There is no statistically significant difference between the X-ray luminosity functions of *HRI*-detected Class II and Class III sources, i.e. T Tauri stars with and without disks, confirming that the contribution of these disks to X-ray absorption, or emission (for instance by magnetic reconnection between the star and the disk), must be small.
- (4) X-ray variability of *HRI*-detected T Tauri stars has been studied by comparing the *HRI* data with the previously obtained *PSPC* data, and using *HRI* observations done at three different epochs. The resulting statistics show that most of the sources are variable, and that their X-ray variability is consistent with a solar-like (hence magnetic) flare origin.
- (5) We use the information given both by the *ISOCAM* survey and by our *HRI* deep exposure to study the T Tauri star population of the ρ Oph dense cores. We confirm that essentially all Class II and Class III YSO are X-ray emitters, and that a strong correlation ($\log(L_X/\text{erg s}^{-1}) = (1.0 \pm 0.2) \times \log(L_*/L_{\odot}) + 30.1$) exists between the X-ray luminosity and the stellar luminosity of T Tauri stars, likely down to low luminosities ($L_* \sim 0.1 L_{\odot}$). We confirm that the characteristic L_X/L_* for T Tauri stars is $\sim 10^{-4}$ in the ρ Oph cloud, albeit with a large dispersion. There is no evidence for a magnetic “saturation” seen at a level of 10^{-3} in late-type main sequence stars.
- (6) However, most of the new *ISOCAM* Class II sources are not detected by the *HRI*. We show that this is consistent with their intrinsic X-ray luminosities being too faint if “predicted” using the above L_X – L_* correlation.

7.2. What have we learned ?

- (1) The first general conclusion we can draw from the *HRI* results presented above is a complete confirmation of the *PSPC* results obtained by CMFA. This was not *a priori* obvious, since the CMFA population (*PSPC* and

near-IR) overlaps, but is different from, the *HRI*/near-IR/*ISOCAM* population presented in this paper: many *PSPC* sources are not detected by the *HRI* (see Appendix C), and some *HRI* sources are Class II and Class III newly classified thanks to a combined identification with *ISOCAM*. This shows that the L_X-L_* correlation is robust for the ρ Oph TTS.

- (2) The second, and perhaps most important, conclusion is the probable existence of ~ 40 unknown X-ray YSO down to a limit of $L_X \sim 3 \times 10^{28} \text{ erg s}^{-1}$ in the *HRI/ISOCAM* overlapping area, which should be mainly low- to very low-mass ($< 0.1\text{--}0.6 M_\odot$) diskless, “Class III TTS”. This prediction is based both on the use of the L_X-L_* correlation, legitimated by its robustness, and on the discovery of a large number of faint new IR sources by *ISOCAM*. As shown below, it may be soon verified by the next generation of X-ray satellites, namely *XMM-Newton* and *Chandra*. In this respect, the present paper can be taken as a “transition” paper between two generations of X-ray satellites.

Why is the detection of these “unknown TTS” important? Because they are diskless, they are unlikely to be recognized as YSO by IR observations alone; and because they are likely to be as numerous as the YSO with IR excess, they have to be included in any reliable census of YSO, with an impact on such basic quantities as the initial mass function, or the star formation efficiency, especially if considered from an evolutionary point of view. For instance, from the results in this paper it is impossible to study the real connection between the distributions of the Class II and Class III sources in the densest regions, in particular to see whether the distribution of the Class III sources is also centered on the same DCO⁺ cores as the Class II sources. The number of Class III sources embedded in the densest regions may, or may not, be comparable to that of the Class II sources, depending on the timescale for disk dispersal, especially among low-mass YSO. An X-ray improved census of Class III sources may also be crucial in determining whether a burst of star formation is presently going on in the ρ Oph cores, as some recent indications suggest (see Martín et al. 1998). It will also allow to study the L_X-L_* correlation for Class III and Class II sources separately, which was not possible in this paper (§) due to insufficient statistics.

7.3. The potential of *XMM-Newton* and *Chandra*

To quantify the prospects for improvement in the X-ray domain, we have computed the detection threshold for the X-ray camera *EPIC* aboard *XMM-Newton*, which was successfully launched in December 1999 (see Fig. 7). The improved sensitivity and enlarged energy range (0.5–12 keV) of *EPIC* will allow to detect the weak *ISOCAM* Class II sources, and also to discover numerous unknown faint or embedded Class III sources, in particular if they have high

plasma temperatures (several keV) reached during flares, and extend the census of this population towards the low-mass end. In the best case, the *XMM-Newton* sensitivity will reach $L_X \sim 10^{28} \text{ erg s}^{-1}$ for $A_V \gtrsim 20$, for long exposures (>75 ksec). This is nearly two orders of magnitude more sensitive than *ROSAT*. In case the faint Class III sources turn out to be so crowded that confusion problems arise, the excellent angular resolution of *Chandra* will be critical.

In ρ Oph, there are already several identified *bona fide* and candidate brown dwarfs (see review in Neuhäuser et al. 1999, and references therein), and four of them have been recently detected in X-ray using the *ROSAT PSPC* archive (Neuhäuser et al. 1999). Neuhäuser et al. have also shown that brown dwarfs could be X-ray emitters with the same ratio $\log(L_X/L_*) \sim -4$ than for T Tauri stars. Thus *Chandra* and *XMM-Newton* should be able to detect many more of these objects with low stellar luminosity and masses, shedding a new light on their nature and early evolution.

Acknowledgements. We thank Francesco Palla for fruitful discussions during the 5th French-Italian meeting in the island of Ponza, and the referee Fred Walter for his useful remarks. NG is supported by the European Union (Marie Curie Individual grant; HPMF-CT-1999-00228). EDF is partially supported by NASA contract NAS8-38252. We used SIMBAD maintained by the CDS (Strasbourg Observatory, France). We also used photographic data obtained using The UK Schmidt Telescope: original plate material is copyright © of the ROE and the AAO.

Appendix A: HRI X-ray source detection

Source detection was done using EXSAS (Zimmermann et al. 1997), and the standard command DETECT/SOURCES. This command generates a local source detection by a sliding-window technique followed by a maximum likelihood test which compares the observed count distribution on the full resolution image (pixel of 0.5'') to a model of the point spread function (PSF) and the local background (Crudace et al. 1988). The “likelihood of existence” is defined as $\mathcal{L} = -\ln P_0$, where P_0 the probability of the null hypothesis that the observed distribution of counts is only due to a statistical background fluctuation; \mathcal{L} provides a maximum likelihood measure for the presence of a source above the local background. We take $\mathcal{L}=6.8$ as detection threshold ($P_0 \leq 0.0011$; or $\geq 3.25 \sigma$ for Gaussian statistics) as argued in CMFA.

For source detection, the *HRI* report (David 1997) advises to screen out lower and higher *HRI* Pulse Height Analyzer (hereafter PHA) channels, which are found to have the highest background. However, source counts should always be determined using all the 1–15 channels to cancel out the uneven *HRI* efficiency distribution across the detector area (S. Döbereiner, private communication). We

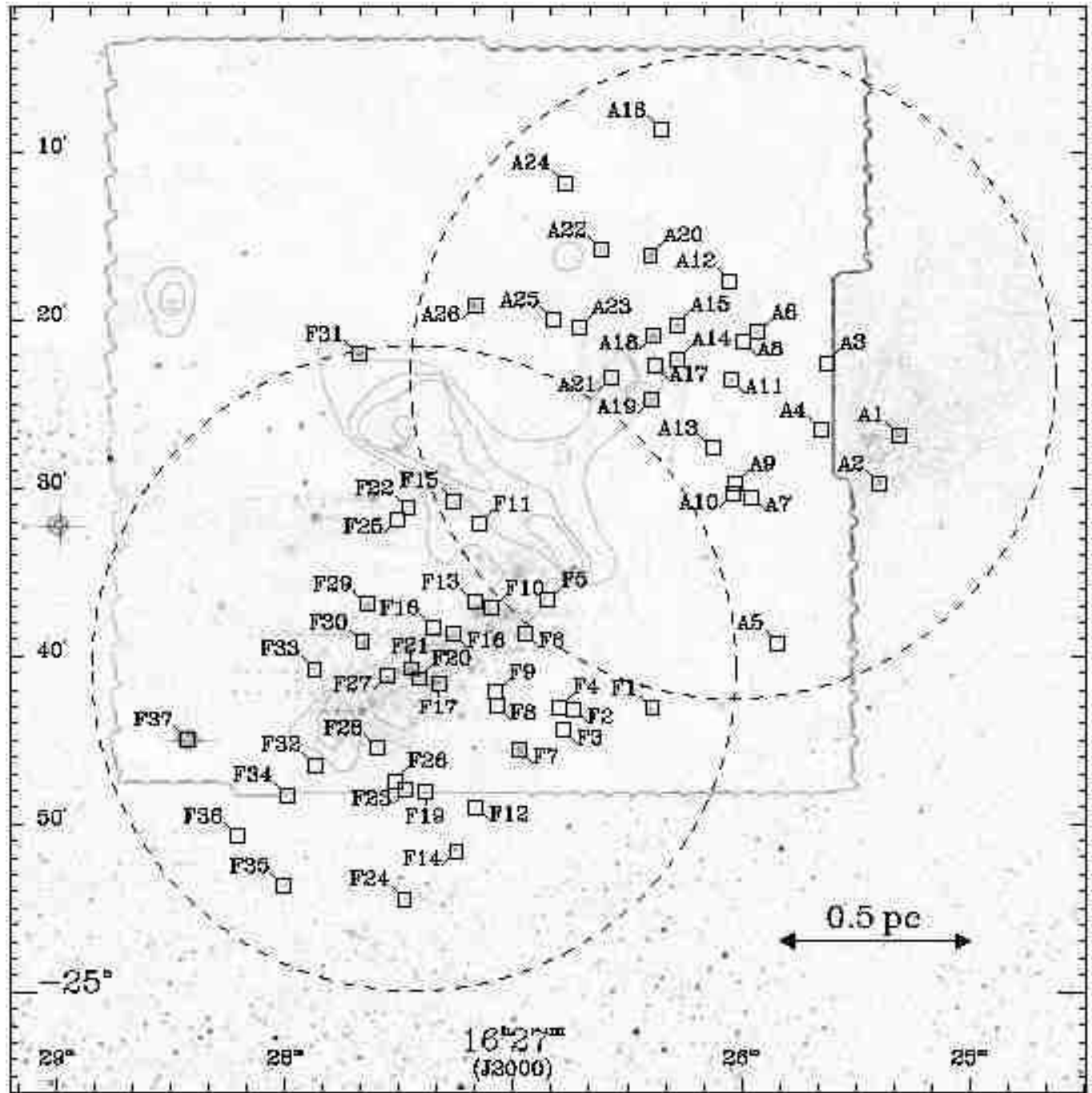


Fig. A.1. Sources designations from Table A.1–B.1. The image of Fig. 2 was smoothed using an edge detection algorithm.

decided to search X-ray sources above a fixed detection threshold in channels 1–15 and 3–8.¹⁶ EXSAS gave us list

¹⁶ In the core F image #3, many 1–15 channel detections with high \mathcal{L} were not found in the 3–8 channel band. Thus, we decided to take channels 2–8 instead of 3–8 in the three exposures. This third observation was the last of our program, one year after the Core A observation (see Table 1). According to Prestwich et al. (1998), the mean pulse height decreases by 0.5 channels year⁻¹: this effect might explain why we must

of X-ray detections with positions, one sigma error box (σ_X), \mathcal{L} , and count rate. We removed sources detected in channels 1–15 but not in 3–8, considering these detections as spurious. For instance, there are two hot spots in the Core A observation in the South-East corner of the *HRI*.

decrease the lower channel boundary from 3 to 2. The upper channel boundary seems to be less sensitive, probably due to fewer counts in upper channels (see David et al. 1997).

Since hot spots are usually considered as spurious detections, this criterion automatically removes them.

The astrometry must be corrected from offsets of typically a few arcseconds due to the time-dependent boresight error in the *ROSAT* aspect system. To do this, IR or optical counterparts in a $10''$ radius circle around the X-ray sources were searched. We then selected a sample of X-ray sources with an unambiguous counterpart and $1\sigma_X$ (half width) error box $\leq 1''$, comparable to the IR/optical typical position error box ($\sigma_* \sim 1''$). Then, offsets in right ascension (α) and declination (δ) were estimated by individual offset weighted mean: $\alpha_{offset} = \sum_{i=1}^n w_i \times (\alpha_{X,i} - \alpha_{*,i})$, $\delta_{offset} = \sum_{i=1}^n w_i \times (\delta_{X,i} - \delta_{*,i})$, with $w_i = (1/\sigma_{X,i} + 1/\sigma_{*,i}) / \sum_{i=1}^n (1/\sigma_{X,i} + 1/\sigma_{*,i})$. We found offsets ranging from $-0.5''$ to $2.5''$. We subtracted these offsets, and checked the quality of our astrometry by estimating sample residuals mean before and after offsets subtraction: $\sigma_{shift} = \frac{1}{n} \times \sum_{i=1}^n \sqrt{(\alpha_{X,i} - \alpha_{*,i} - \alpha_{offset})^2 + (\delta_{X,i} - \delta_{*,i} - \delta_{offset})^2}$. We found σ_{shift} ranging from $0.5''$ to $1.2''$. σ_{shift} and σ_* ($= 1.2''$) were then quadratically added to σ_X to obtain an error box radius after astrometric correction ($\sigma_{total}^2 = \sigma_X^2 + \sigma_{shift}^2 + \sigma_*^2$). In the case of the three different core F observations, the images were aligned and merged after astrometric correction to obtain a single deep *HRI* exposure of 77.2 ks. Source detection was subsequently performed as described in the article.

Table A.1 lists the *HRI* X-ray sources, for which we adopt, in Col. 1, the same acronym as in CMFA: “ROXR” (for ρ Oph X-ray *ROSAT* source), followed by “A” or “F”.¹⁷ Fig. A.1 indicates the source numbering.

In order to allow easier comparisons with previous work, X-ray source positions are listed in both J2000 and B1950 equinoxes, with their $1\sigma_{total}$ error box, in Cols. 2–6. The likelihood of existence \mathcal{L} is in Col. 7. Count rates are indicated in Col. 8–11. For the core F field, the indicated positions (α, δ) and \mathcal{L} values correspond to observation (#1, #2, or #3) where \mathcal{L} and the position accuracy are the best, i.e. when the count rate is highest. When an X-ray source is detected in one observation above the detection threshold, and not detected in other observations, we have estimated the corresponding count rate upper limits (3.25σ), using the EXSAS command COMPUTE/UPPER_LIMITS. We have noted that the detection efficiency degrades with increasing angle to the axis, in the same way as the point spread function (this is discussed in §5.2).

¹⁷ The “legal” designation for a new ROSAT source is RXJHHMM.m \pm DDMM, where J stands for coordinates in J2000 and m is the cut (not rounded) decimal value. Our tables do not use this notation for simplicity in the discussion, but the correct designation is easy to reconstruct from the position given if required. For example, ROXRF14 = ROXs20B = RXJ162714-2430.

Appendix B: Optical/IR counterparts of the HRI X-ray sources

We searched stellar counterparts for the 63 *ROSAT HRI* X-ray sources on the ESO/SERC second digitized sky survey (DSS2). Fig. B.1 gives the finding charts with BKLT IR sources for each of the 63 *ROSAT HRI* X-ray sources.

Table B.1 gives identification lists for the two fields, and cross-identification with other surveys. Col. 1 is the ROXR numbering from detection (Table A.1). Cols. 2–4 are respectively cross-identification lists with the X-ray sources of CMFA (ROXR1), Casanova (1994; ROXR2), and Kamata et al. (1997). Dots mean “X-ray source undetected”, and dash “out of observation field”. Col. 5 gives the first name attributed to this counterpart.

In the core A field, we find 26 X-ray sources, of which only one (ROXRA10) remains without optical or IR counterpart. Of the 25 identified X-ray sources, 22 were seen with the *ROSAT PSPC*, and 4 are new detections (ROXRA3, 10, 16, 22). In the core F field, we find 37 X-ray sources, including 7 without optical or IR counterpart. Of the 30 identified X-ray sources, 18 were seen with the *ROSAT PSPC*, and 12 are new detections (ROXRF3, 8, 12, 15, 18, 19, 24, 26, 28, 32, 35, 36). Altogether, 63 X-ray sources are detected, and 55 are identified. Of the 55 identified X-ray sources 40 are *PSPC* sources.

For sources with a low statistical significance ($6.8 \leq \mathcal{L} \leq 9.1$, or $10^{-4} \leq P_0 \leq 1.1 \times 10^{-3}$; $3.25\text{--}3.9\sigma$ for Gaussian statistics) we find X-ray sources with and without optical or IR counterparts. The X-ray sources without counterparts are always weak sources and may be spurious detections (locally high background), and this may therefore also be the case for weak X-ray sources with counterparts in case of chance spatial coincidence. For instance in the Core A field (respectively Core F) there are 875 (resp. 1173) BKLT sources; this sample is dominated by background sources without detectable X-ray emission. To estimate the number of chance coincidences, we have placed in each field 10^5 random X-ray source positions, and searched for each whether there is a BKLT source in a circle of $10''$ radius: we have then an estimate of the probability to find a BKLT counterpart by chance within $10''$ from a spurious X-ray detection. This probability is 0.044 (resp. 0.049) for Core A (resp. Core F), or approximately 1/20 for both; in other words one (resp. two) spurious source identification are expected for the Core A (resp. Core F) field. As we have for Core A (resp. Core F) two (resp. 15) X-ray sources with $\mathcal{L} \leq 9.1$ out of 26 (resp. out of 37), this implies that one weak X-ray source in Core A (resp. 13 in Core B) is real, which is consistent with the number of identifications. We are therefore confident that the identifications of weak X-ray sources with stellar counterparts are correct.

Table A.1. *HRI* X-ray sources in the ρ Oph cloud cores A & F.

ROXR	J2000		B1950		\pm	\mathcal{L}	COUNT RATE			
	α	δ	α	δ			#1	#2	#3	#1+2+3
(1)	(2)	(3)	(4)	(5)	(6)	(7)	[cts/ks] (8)	[cts/ks] (9)	[cts/ks] (10)	[cts/ks] (11)
A1	16 ^h 25 ^m 19 ^s .0	-24°26'52''	16 ^h 22 ^m 17 ^s .6	-24°20'04''	2	5765.4	40.7±0.9			
A2	16 ^h 25 ^m 24 ^s .2	-24°29'47''	16 ^h 22 ^m 22 ^s .7	-24°22'59''	3	15.4	0.8±0.2			
A3	16 ^h 25 ^m 38 ^s .0	-24°22'35''	16 ^h 22 ^m 36 ^s .7	-24°15'47''	2	18.5	0.4±0.1			
A4	16 ^h 25 ^m 39 ^s .4	-24°26'36''	16 ^h 22 ^m 38 ^s .0	-24°19'49''	2	20.0	0.6±0.1			
A5	16 ^h 25 ^m 50 ^s .6	-24°39'16''	16 ^h 22 ^m 48 ^s .9	-24°32'29''	2	742.2	16.1±0.7			
A6	16 ^h 25 ^m 56 ^s .0	-24°20'47''	16 ^h 22 ^m 54 ^s .7	-24°14'01''	2	101.2	1.9±0.2			
A7	16 ^h 25 ^m 57 ^s .5	-24°30'34''	16 ^h 22 ^m 56 ^s .0	-24°23'48''	2	231.1	3.0±0.3			
A8	16 ^h 25 ^m 59 ^s .6	-24°21'20''	16 ^h 22 ^m 58 ^s .3	-24°14'34''	2	23.0	0.7±0.2			
A9	16 ^h 26 ^m 01 ^s .6	-24°29'47''	16 ^h 23 ^m 00 ^s .1	-24°23'01''	2	16.8	0.5±0.1			
A10	16 ^h 26 ^m 02 ^s .3	-24°30'26''	16 ^h 23 ^m 00 ^s .8	-24°23'40''	3	8.8	0.4±0.1			
A11	16 ^h 26 ^m 02 ^s .9	-24°23'35''	16 ^h 23 ^m 01 ^s .6	-24°16'50''	2	3581.6	24.1±0.7			
A12	16 ^h 26 ^m 03 ^s .2	-24°17'45''	16 ^h 23 ^m 01 ^s .9	-24°10'59''	2	47.4	1.0±0.2			
A13	16 ^h 26 ^m 07 ^s .7	-24°27'41''	16 ^h 23 ^m 06 ^s .2	-24°20'55''	2	19.4	0.7±0.2			
A14	16 ^h 26 ^m 16 ^s .8	-24°22'22''	16 ^h 23 ^m 15 ^s .5	-24°15'37''	2	169.1	2.5±0.2			
A15	16 ^h 26 ^m 17 ^s .1	-24°20'20''	16 ^h 23 ^m 15 ^s .7	-24°13'36''	2	235.1	2.9±0.3			
A16	16 ^h 26 ^m 21 ^s .3	-24°08'45''	16 ^h 23 ^m 20 ^s .2	-24°02'01''	5	12.5	1.3±0.3			
A17	16 ^h 26 ^m 22 ^s .7	-24°22'49''	16 ^h 23 ^m 21 ^s .3	-24°16'04''	3	7.9	0.3±0.1			
A18	16 ^h 26 ^m 23 ^s .4	-24°20'59''	16 ^h 23 ^m 22 ^s .1	-24°14'14''	2	95.1	1.4±0.2			
A19	16 ^h 26 ^m 23 ^s .9	-24°24'47''	16 ^h 23 ^m 22 ^s .5	-24°18'02''	3	10.5	0.4±0.1			
A20	16 ^h 26 ^m 24 ^s .1	-24°16'11''	16 ^h 23 ^m 22 ^s .8	-24°09'27''	2	18.9	0.7±0.2			
A21	16 ^h 26 ^m 34 ^s .2	-24°23'26''	16 ^h 23 ^m 32 ^s .8	-24°16'43''	2	54.7	1.0±0.2			
A22	16 ^h 26 ^m 36 ^s .9	-24°15'53''	16 ^h 23 ^m 35 ^s .7	-24°09'10''	3	10.9	0.6±0.2			
A23	16 ^h 26 ^m 42 ^s .8	-24°20'29''	16 ^h 23 ^m 41 ^s .5	-24°13'46''	3	13.1	0.6±0.2			
A24	16 ^h 26 ^m 46 ^s .4	-24°11'54''	16 ^h 23 ^m 45 ^s .2	-24°05'12''	3	57.1	3.0±0.4			
A25	16 ^h 26 ^m 49 ^s .2	-24°20'02''	16 ^h 23 ^m 47 ^s .9	-24°13'19''	3	18.0	1.1±0.2			
A26	16 ^h 27 ^m 09 ^s .9	-24°19'15''	16 ^h 24 ^m 08 ^s .6	-24°12'34''	6	9.7	1.2±0.3			
F1	16 ^h 26 ^m 23 ^s .5	-24°43'10''	16 ^h 23 ^m 21 ^s .7	-24°36'26''	3	54.8	2.2 ± 0.7	<1.2	3.3 ± 0.4	2.0 ± 0.3
F2	16 ^h 26 ^m 44 ^s .0	-24°43'14''	16 ^h 23 ^m 42 ^s .2	-24°36'31''	2	126.9	≤1.4	1.8 ± 0.4	3.1 ± 0.3	2.1 ± 0.2
F3	16 ^h 26 ^m 46 ^s .8	-24°44'28''	16 ^h 23 ^m 45 ^s .0	-24°37'46''	2	25.5	≤0.8	≤0.7	1.2 ± 0.2	0.7 ± 0.1
F4	16 ^h 26 ^m 47 ^s .8	-24°43'05''	16 ^h 23 ^m 46 ^s .1	-24°36'23''	3	7.1			0.3 ± 0.1	0.3 ± 0.1
F5	16 ^h 26 ^m 50 ^s .8	-24°36'43''	16 ^h 23 ^m 49 ^s .1	-24°30'01''	3	6.8	≤1.0	0.5 ± 0.2	≤0.3	≤0.2
F6	16 ^h 26 ^m 56 ^s .9	-24°38'42''	16 ^h 23 ^m 55 ^s .1	-24°32'00''	2	9.1	≤0.5	≤0.4	0.4 ± 0.1	0.2 ± 0.1
F7	16 ^h 26 ^m 58 ^s .4	-24°45'36''	16 ^h 23 ^m 56 ^s .5	-24°38'55''	2	60.1	0.8 ± 0.3	2.3 ± 0.3	1.0 ± 0.2	1.3 ± 0.1
F8	16 ^h 27 ^m 04 ^s .3	-24°43'00''	16 ^h 24 ^m 02 ^s .5	-24°36'19''	2	11.4	≤0.9	≤0.7	0.4 ± 0.1	0.4 ± 0.1
F9	16 ^h 27 ^m 04 ^s .5	-24°42'13''	16 ^h 24 ^m 02 ^s .7	-24°35'32''	2	25.6	0.7 ± 0.3	0.4 ± 0.2	1.0 ± 0.2	0.8 ± 0.1
F10	16 ^h 27 ^m 05 ^s .6	-24°37'14''	16 ^h 24 ^m 04 ^s .0	-24°30'33''	3	8.8			0.2 ± 0.1	0.2 ± 0.1
F11	16 ^h 27 ^m 08 ^s .9	-24°32'11''	16 ^h 24 ^m 07 ^s .3	-24°25'29''	3	6.9	≤1.2	0.5 ± 0.2	≤0.3	≤0.2
F12	16 ^h 27 ^m 09 ^s .7	-24°49'02''	16 ^h 24 ^m 07 ^s .8	-24°42'21''	4	8.9			0.4 ± 0.1	0.4 ± 0.1
F13	16 ^h 27 ^m 10 ^s .1	-24°36'50''	16 ^h 24 ^m 08 ^s .4	-24°30'09''	2	8.9	≤0.6	≤0.2	0.3 ± 0.1	≤0.2
F14	16 ^h 27 ^m 14 ^s .9	-24°51'40''	16 ^h 24 ^m 12 ^s .9	-24°44'59''	2	140.2	3.6 ± 0.7	4.4 ± 0.5	4.3 ± 0.4	4.2 ± 0.3
F15	16 ^h 27 ^m 15 ^s .5	-24°30'49''	16 ^h 24 ^m 13 ^s .9	-24°24'08''	6	7.1	≤0.9	≤0.4	1.0 ± 0.3	≤0.3
F16	16 ^h 27 ^m 15 ^s .8	-24°38'42''	16 ^h 24 ^m 14 ^s .1	-24°32'01''	2	15.1	≤0.5	0.7 ± 0.2	0.3 ± 0.1	0.5 ± 0.1
F17	16 ^h 27 ^m 19 ^s .5	-24°41'40''	16 ^h 24 ^m 17 ^s .6	-24°35'00''	1	1648.5	16.6 ± 1.2	13.8 ± 0.7	14.4 ± 0.6	13.2 ± 0.4
F18	16 ^h 27 ^m 20 ^s .7	-24°38'23''	16 ^h 24 ^m 19 ^s .0	-24°31'43''	2	6.9	≤0.2	≤0.1	0.3 ± 0.1	≤0.1
F19	16 ^h 27 ^m 22 ^s .9	-24°48'07''	16 ^h 24 ^m 20 ^s .9	-24°41'27''	2	12.6	≤0.5	≤0.3	0.5 ± 0.2	≤0.3
F20	16 ^h 27 ^m 24 ^s .8	-24°41'24''	16 ^h 24 ^m 23 ^s .0	-24°34'44''	2	7.2	≤0.3	0.3 ± 0.1	≤0.2	≤0.2
F21	16 ^h 27 ^m 26 ^s .9	-24°40'49''	16 ^h 24 ^m 25 ^s .0	-24°34'09''	2	62.0	3.2 ± 0.6	≤0.1	≤0.2	0.7 ± 0.1
F22	16 ^h 27 ^m 27 ^s .4	-24°31'15''	16 ^h 24 ^m 25 ^s .8	-24°24'35''	2	482.8	≤1.4	11.1 ± 0.7	0.6 ± 0.2	4.3 ± 0.3
F23	16 ^h 27 ^m 28 ^s .1	-24°48'04''	16 ^h 24 ^m 26 ^s .2	-24°41'25''	3	7.1			0.2 ± 0.1	0.2 ± 0.1
F24	16 ^h 27 ^m 28 ^s .6	-24°54'31''	16 ^h 24 ^m 26 ^s .5	-24°47'51''	5	12.8	2.4 ± 0.6	≤1.2	1.4 ± 0.3	1.2 ± 0.2
F25	16 ^h 27 ^m 30 ^s .1	-24°31'55''	16 ^h 24 ^m 28 ^s .4	-24°25'15''	3	7.3	≤0.6	0.5 ± 0.2	≤0.3	≤0.3
F26	16 ^h 27 ^m 31 ^s .1	-24°47'30''	16 ^h 24 ^m 29 ^s .1	-24°40'50''	2	13.2	0.8 ± 0.3	0.6 ± 0.2	≤0.3	0.7 ± 0.1
F27	16 ^h 27 ^m 33 ^s .2	-24°41'14''	16 ^h 24 ^m 31 ^s .4	-24°34'35''	2	48.6	≤0.7	0.9 ± 0.2	1.3 ± 0.2	1.0 ± 0.1
F28	16 ^h 27 ^m 35 ^s .5	-24°45'32''	16 ^h 24 ^m 33 ^s .7	-24°38'53''	3	7.4			0.2 ± 0.1	0.2 ± 0.1
F29	16 ^h 27 ^m 38 ^s .3	-24°36'58''	16 ^h 24 ^m 36 ^s .6	-24°30'19''	2	333.4	9.6 ± 0.9	0.5 ± 0.2	0.5 ± 0.1	1.9 ± 0.2
F30	16 ^h 27 ^m 39 ^s .5	-24°39'15''	16 ^h 24 ^m 37 ^s .7	-24°32'35''	1	61.5	1.5 ± 0.4	1.4 ± 0.3	1.1 ± 0.2	1.2 ± 0.1
F31	16 ^h 27 ^m 40 ^s .4	-24°22'05''	16 ^h 24 ^m 39 ^s .0	-24°15'26''	3	434.4	10.1 ± 1.1	2.1 ± 0.5	12.3 ± 0.7	7.3 ± 0.4
F32	16 ^h 27 ^m 51 ^s .9	-24°46'31''	16 ^h 24 ^m 50 ^s .0	-24°39'53''	2	7.7			0.3 ± 0.1	0.3 ± 0.1
F33	16 ^h 27 ^m 52 ^s .1	-24°40'49''	16 ^h 24 ^m 50 ^s .3	-24°34'11''	1	199.4	2.9 ± 0.5	2.7 ± 0.3	2.9 ± 0.3	2.8 ± 0.2
F34	16 ^h 27 ^m 59 ^s .3	-24°48'19''	16 ^h 24 ^m 57 ^s .3	-24°41'42''	5	7.0	≤1.2	0.8 ± 0.3	≤0.6	≤0.5
F35	16 ^h 28 ^m 00 ^s .1	-24°53'44''	16 ^h 24 ^m 58 ^s .0	-24°47'07''	3	59.4	≤2.8	≤1.9	3.7 ± 0.5	2.5 ± 0.3
F36	16 ^h 28 ^m 12 ^s .3	-24°50'47''	16 ^h 25 ^m 10 ^s .2	-24°44'10''	4	31.9	≤2.2	≤1.6	2.4 ± 0.4	1.7 ± 0.2
F37	16 ^h 28 ^m 25 ^s .3	-24°45'00''	16 ^h 25 ^m 23 ^s .3	-24°38'24''	3	47.4	2.5 ± 0.6	3.5 ± 0.5	1.8 ± 0.3	2.6 ± 0.3

Notes: \pm gives the $1\sigma_{total}$ error box; \mathcal{L} is the likelihood of existence, we give the maximum value for the observation set.

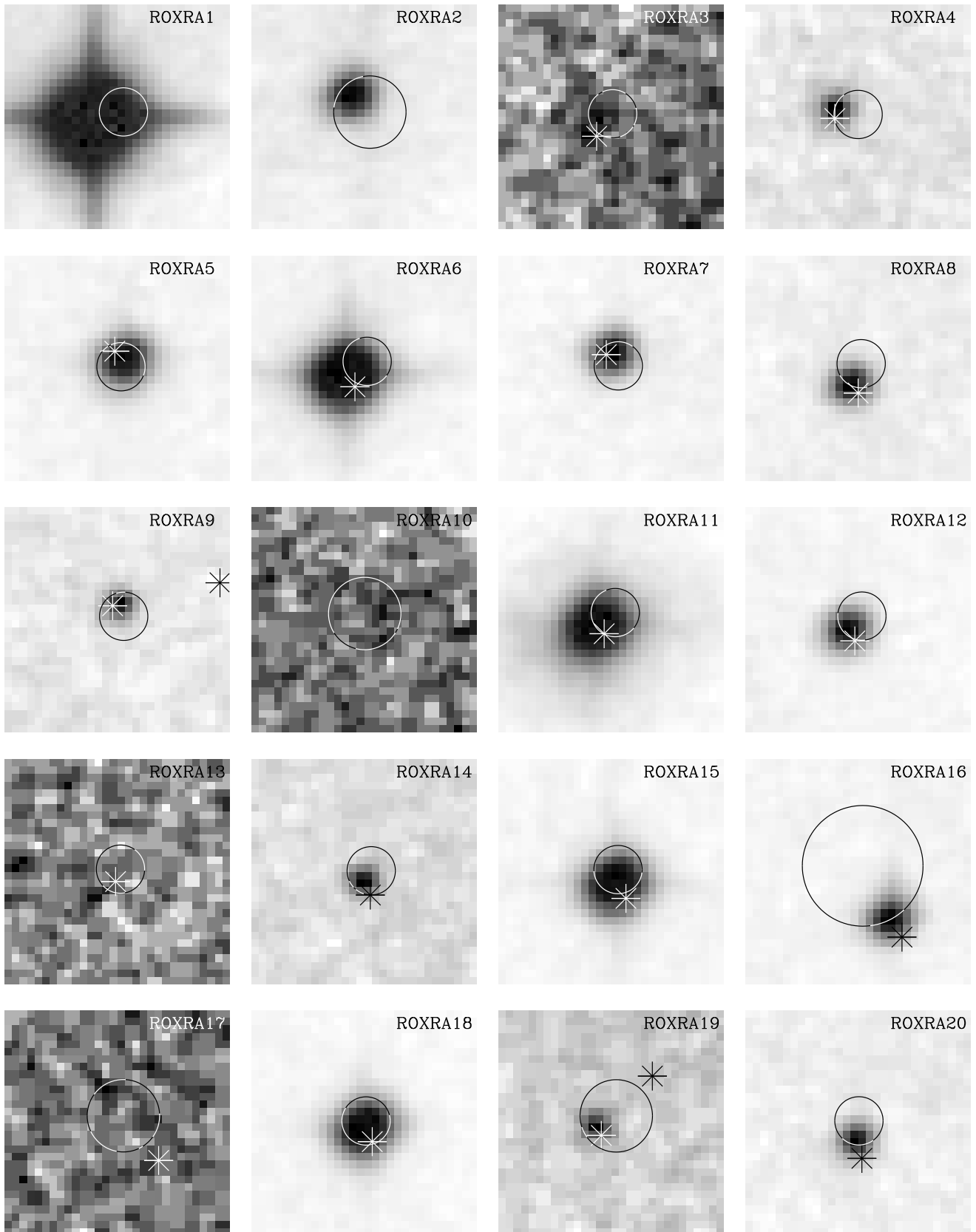
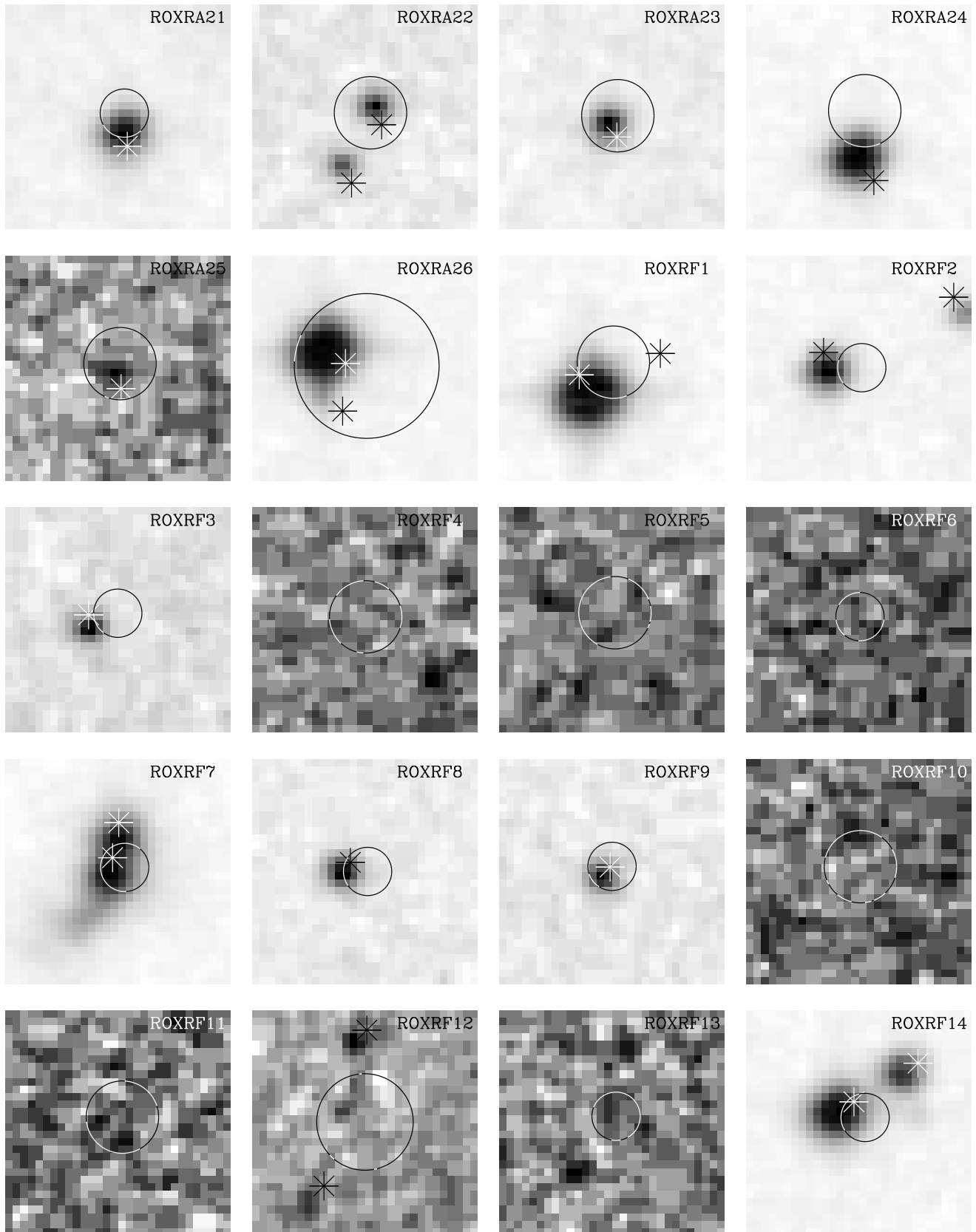


Fig. B.1. Optical finding charts of the 63 *ROSAT HRI* X-ray sources of Tables A.1 and B.1. Each map is a $30'' \times 30''$ extracted from the ESO/SERC sky survey red Schmidt plate using the second Digitized Sky Survey (one pixel= $1''$); North is at the top, East at the left. Circles show the *ROSAT HRI* 90% confidence error boxes (i.e. one sigma error box from Table A.1 multiplied by 1.6). Asterisks show the BKL T infrared sources 90% confidence error boxes ($\sim 1.9''$).

**Fig. B.1.** *continued.*

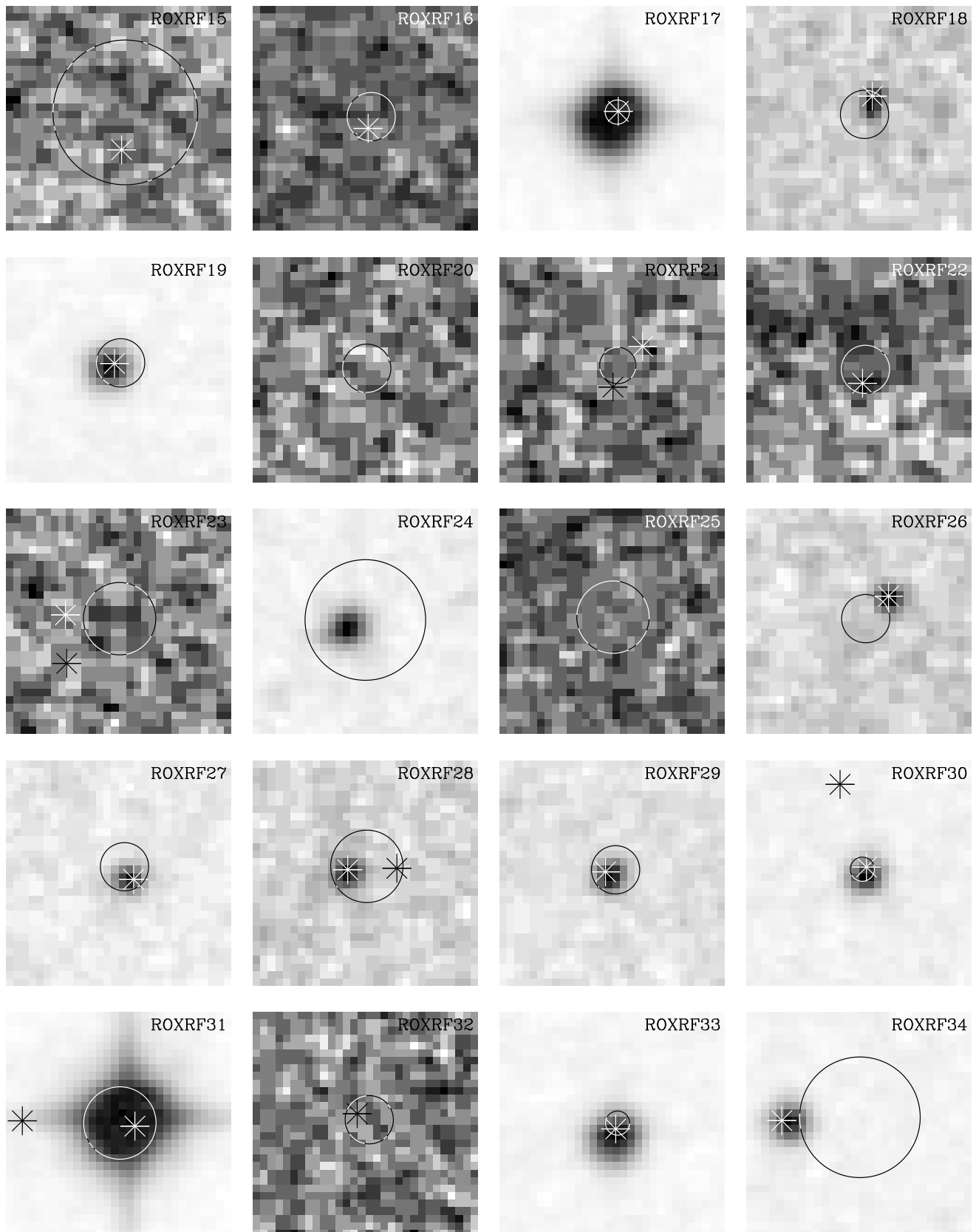
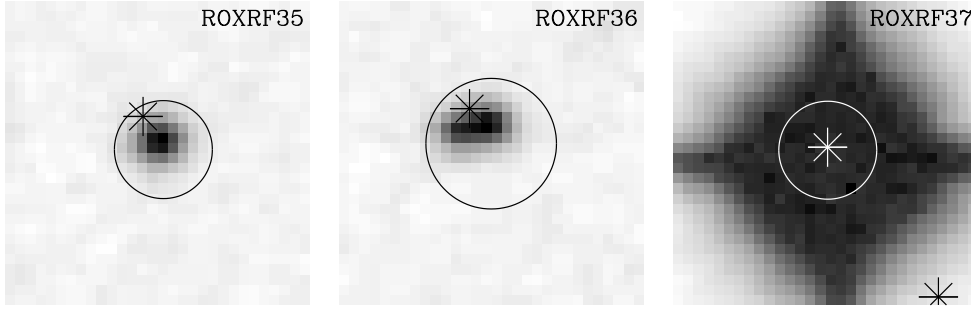


Fig. B.1. *continued.*

Fig. B.1. *continued.*

Appendix C: Comparison between *HRI* and *PSPC* observations

Within the boundaries of our observation fields (core A and core F), there are 61 X-ray sources detected previously with the *ROSAT PSPC* (53 from CMFA, and 8 from Casanova 1994). However, 21 X-ray sources are not detected with the *ROSAT HRI*. This difference could be explained by lower observational sensitivity and/or source variability. To elucidate this point, we must estimate *HRI* count rates for *PSPC* sources, and compare them with the adopted *HRI* detection threshold (3.25σ).

We first estimate the conversion factor between the *PSPC* count rate in the energy range of CMFA (1.0–2.4 keV) and the *HRI* count rate in the whole energy range (0.1–2.4 keV). We did not select X-ray sources with ambiguous *PSPC* detection (10 sources with notes in Cols. 2–3 of Table B.1). For core F observation, the lowest detection count rate was taken to minimize variability effects (four sources with upper limits are not selected): we kept only 26 X-ray sources. Since many of these sources are variable (as shown by the core F observations), a conversion factor estimator insensitive to extreme values of the sample is needed. This is why we take the median of the *PSPC/HRI* count rate ratio, instead of the mean. We find $PSPC_{1-2.4\text{keV}}$ count rate = $2.4 \times HRI_{0.1-2.4\text{keV}}$ count rate.

Fig. C.1 displays the *HRI* $_{0.1-2.4\text{keV}}$ count rate vs. the *PSPC* $_{1-2.4\text{keV}}$ count rate. It shows two classes of sources: sources near the median, and sources beyond the median (with error bars). The dispersion of points (within 1 rms) around the median value could be due to X-ray extinction effect on the conversion factor or to a variability factor ≤ 2 . Preibisch et al. (1996) calculated the conversion for the whole energy band of the *ROSAT HRI* assuming optically thin plasma emission with $T_X = 10^7$ K and different values for the X-ray extinction: for N_H increasing from $6.5 \times 10^{19} \text{ cm}^{-2}$ to 10^{22} cm^{-2} , the conversion factor decreases from 2.5 to 2.0. Our observational estimate is in agreement with these values, which also show that the dependence of the conversion factor on X-ray extinction is small compared to the dispersion of count rates and can be neglected in our plot. We conclude that the dispersion

is due to variability: WL20, GSS37, VSS27, and SR9 must have been in a high state during the *PSPC* observation, as were ROXs4 and SR2 during the *HRI* observation, the other sources being essentially unchanged in both observations.

Using this conversion factor, we can estimate the *HRI* count rate from the *PSPC* count rate, and compare it with our *HRI* threshold computed with EXSAS. We find that 14 sources are below this threshold (ROXR1-1, 6, 7, 16, 20, 21, 27, 33, 34, 37, 40, 53, and ROXR2-16, 18), and the other 7 sources were in a high state during the *PSPC*

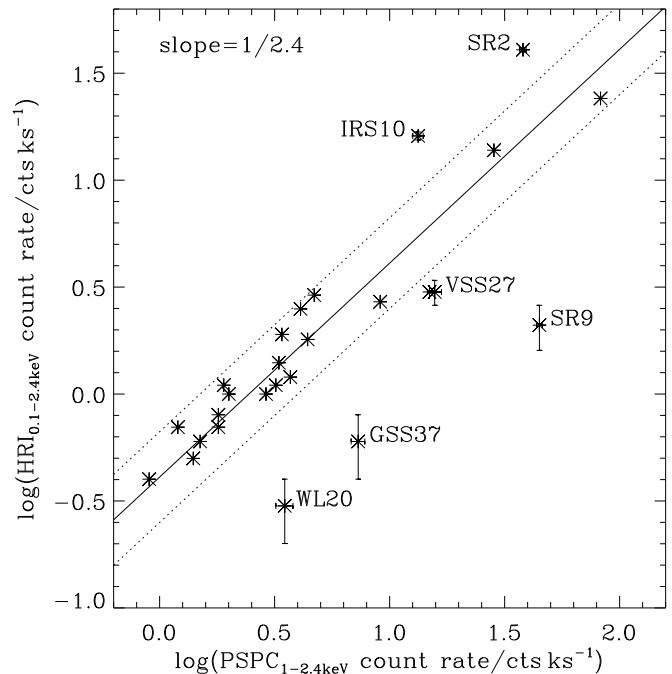


Fig. C.1. Plot of *ROSAT HRI* (this paper) vs. *PSPC* (CMFA) count rates and sources variability. The dashed line is the median value of the conversion factor between *HRI* and *PSPC* count rates (2.4); dotted lines show the dispersion (1 rms) around this median value. Count rate error boxes are shown for sources outward the dotted lines. Sources below (above) the dotted lines presumably flared during *PSPC* (*HRI*) observations (see text for details).

Table B.1. *HRI* X-ray sources counterpart identifications in the ρ Oph cloud cores A & F.

ROXR				NAME	ISO	IR Class	A_V [mag]	L_* [L_\odot]	$\log L_X$ (d=140 pc)				
(1)	1 (2)	2 (3)	ASCA (4)						(5)	(6)	(7)	(8)	(9)
A1	2	—	—	SR2=SAO184375	—	III*	0*	1.2*	30.4				
A2	3	—	SR22	—	II*	1.5*	0.4*	29.4				
A3	..	—	B162538-242238	red	nII	10.9	0.2	30.3				
A4	5*	—	IRS3	red	nII	4.6	0.3	29.8				
A5	8	—	1	ROXs4=IRS10	blue	nIII	5.4	1.7	31.4				
A6	9	—	SR4	red	II	1.9	1.5	29.9				
A7	10	—	2	GSS20	blue	III	4.7	1.1	30.5				
A8	11	—	Chini8*=SKS3	...	nIII*	0.5	0.2	29.1				
A9	12*	—	B162601-242945	blue	nIII	8.1	0.5	30.2				
A10	..	—	?				
A11	13	—	3	DoAr21=ROXs8	blue	III	6.0	14.7	31.6				
A12	14	—	VSSG19	blue	nIII	3.9	0.5	29.9				
A13	15*	—	ROXC1=B162607-242742	blue	nIII	20.6	0.7	31.3				
A14	18	—	GSS29	red	II	9.4	1.4	31.0				
A15	17	—	DoAr24=ROXs10A	red	II	1.8	0.7	30.0				
A16	—	..*	—	WSB28	blue	nIII	4.3	0.4	30.1				
A17	22*	—	GSS30-IRS2	blue	III	19.5	0.9	30.9				
A18	24	—	4	GSS31	red	II	6.1	5.9	30.4				
A19	25	—	C3	S2	red	II	11.8	3.7	30.4				
A20	26	—	El24	red	II	10.0	4.5	30.5				
A21	28	—	5	S1=ROXs14	blue	III*	12*	1100*	30.8				
A22	..	—	B162636-241554	red	nII	7.6	0.3	30.2				
A23	29	—	C4	GSS37	red	II	8.5	1.6	30.3				
A24	—	17	VSS27=ROXs16	red	II	5.6	1.9	30.7				
A25	32	—	VSSG3	blue	III	15.7	2.8	31.2				
A26	38	—	SR21*	red	II	3.5	4.0	30.0				
F1	23	—	DoAr25*	red	II	0.7	0.8	29.7	<29.4	29.8	29.6	
F2	31	—	GY112	blue	nIII	3.6	0.4	<30.0	30.2	30.4	30.2	
F3	..	—	GY122	blue	nIII	2.7	0.08	<29.7	<29.6	29.8	29.6	
F4	..	—	<	<	<	?	
F5	..	—	?	?	?	?	
F6	..	—	?	?	?	?	
F7	35*	—	SR24S*	red	II	5.9	2.2	30.1	30.6	30.2	30.3	
F8	..	—	GY193	blue	nIII	7.4	0.3	<30.3	<30.2	30.0	30.0	
F9	36*	—	GY194	blue	nIII	9.1	0.4	30.4	30.2	30.6	30.5	
F10	..	—	<	<	<	?	
F11	..	—	?	?	?	?	
F12	..	—	<i>anonymous star*</i>	—	II-III?	<	<	<	?	
F13	..	—	?	?	?	?	
F14	—	22*	—	ROXs20B	—	III	2.7	0.3	30.3	30.4	30.4	30.4	
F15	..	—	GY238	red	nII	45.7	0.3	<32.9	<32.6	33.0	<32.5	
F16	39	—	WL20	red	II	16.5	0.9	<30.9	31.1	30.7	30.9	
F17	41	—	9A	SR12AB=ROXs21	blue	III	1.2	0.8	30.7	30.6	30.6	30.6	
F18	..	—	B162720-243820	II-III?	?	?	?	?	
F19	..	—	WSB49	..*	II*	1.9	0.2	<29.3	<29.1	29.3	<29.1	
F20	..	—	?	?	?	?	
F21	43*	—	YLW15=IRS43	red	I	30*	10*	32.6	<31.1	<31.4	31.9	
F22	44	—	VSSG25	red	II	9.8	0.4	<30.8	31.7	30.4	31.3	
F23	46*	—	B162728-244803*	—	II-III?	<	<	<	?	
F24	—	..	—	U0600-11613195*	—	II-III?	?	?	?	?	
F25	48*	—	BBRCG50	II-III?	<	<	<	?	
F26	..	—	B162730-244726	blue	nIII	10.3	0.6	30.6	30.5	<30.2	30.5	
F27	49	—	GY292	red	II	10.8	1.6	<30.6	30.7	30.8	30.7	
F28	..	—	GY296*	blue	nIII	5.1	0.08	<	<	<	29.4	
F29	50	—	IRS49	red	II	10.1	1.1	31.6	30.4	30.4	30.9	
F30	51	—	GY314	red	II	6.4	0.8	30.4	30.4	30.3	30.4	
F31	52	—	11	SR9=ROXs29	red	II	0	1.6	29.8	29.2	29.9	29.7	
F32	..	—	GY377	blue	nIII	16.0	0.4	<	<	<	30.6	
F33	54	—	ROXs31=IRS55	blue	III	6.0	1.8	30.7	30.7	30.7	30.7	
F34	55	—	—	WSB58	—	II-III?	?	?	?	?	
F35	—	..	—	B162800-245340	—	II-III?	?	?	?	?	
F36	—	..	—	B162812-245043	—	II-III?	?	?	?	?	
F37	—	34	—	HD148352	blue	III*	0	29.9	30.0	29.8	29.9	

Comments to Table B.1:

* = see notes below. ROXRA or ROXRF = X-ray source number (this article). ROXR1 = CMFA X-ray source number. ROXR2 = Casanova (1994) X-ray source number. ASCA = Kamata et al. (1997) X-ray source number. Dash = out of observation field. Dots = unobserved source. *red* = *ISOCAM* source with IR excess. *blue* = *ISOCAM* source without IR excess. nII = new class II. nIII = new class III. ? = X-ray detected source for which intrinsic X-ray luminosity cannot be determined. \leq = X-ray undetected source. II-III? = class II or class III candidate (see Appendix B).

Notes to Table B.1:

ROXRA1: (7) The IR index ($\alpha_{\text{IR}} = \text{dlog}(\lambda F_{\lambda}) / \text{dlog} \lambda$) is estimated between 2.18–4.69 μm from Walter et al. (1994) and Jensen et al. (1997): we find $\alpha_{\text{IR}} = -2.5$. (8–9) These values are estimated from Walter *et al.* (1994).

ROXRA2: (7) Martín et al. (1998) classify these stars as CTTS. (8–9) These values are estimated from GWAYL.

ROXRA4: (2) ROXR1-5 was identified with IRS3 and IRS5 (CMFA).

ROXRA8: (5) The position of Chini8 (Chini 1981) is 33'' away from this optical star, the good position is given in Table 1 of Strom et al. (1995) by source number 3. (7) The *ISOCAM* LW2 and LW3 upper limits exclude an IR excess (see Appendix D).

ROXRA9: (2) ROXR1-12 was identified with an anonymous optical star (CMFA).

ROXRA13: (2) ROXR1-15 was neither optical nor IR counterpart (CMFA).

ROXRA16: (3) ROXR2-16 was $\sim 1'$ from ROXRA16 (identified with WSB28; CMFA), ie only two error boxes away, but Martín et al. (1998) identify ROXR2-16 with another star.

ROXRA17: (2) ROXR1-22 was identified with GSS30-IRS1, 2, 3 (CMFA).

ROXRA21: (7) S1 is an embedded B-type star (Wilking et al. 1989; André et al. 1988). (8) The visual extinction comes from the data of Lada & Wilking (1984), see André et al. (1988). (9) This B3–B5 stellar luminosity is taken from André et al. (1988).

ROXRA26: (5) In the BKL T survey this well known emission line star appears to be a 6.5'' separation binary (this can also be suspected from the finding chart): the main component is B162710-241914 ($J=8.56$), the second one is B162710-241921 ($J=11.27$).

ROXRF1: (5) The IR star B162623-244308 is also in the 90% confidence error box but its J -band luminosity (15.65) is lower than that of the well known emission line star DoAr25=B162623-244311 (9.29).

ROXRF7: (2) ROXR1-22 was identified with SR24N and SR24S (CMFA). (5) In our observation #2 and #3 the counterpart of ROXRF7 is clearly associated with SR24S. In our observation #1 due to the weakness of the X-ray source the situation is less clear. We associate this source with SR24S.

ROXRF9: (2) ROXR1-36 was ambiguously identified with GY193 and GY194 (CMFA).

ROXRF12: (5) A weak star is visible in the 90% confidence error box on the DSS2 image, but this star is neither detected by the BKL T survey, nor by the PMM USNO-A1.0 catalogue.

ROXRF14: (3) ROXR2-22 was identified with ROXs20A and ROXs20B (CMFA).

ROXRF19: (6) This source is just at the border of the *ISOCAM* survey. As a part of its flux is lost, Bontemps et al. (2000) do not characterize this source. (7) Martín et al. (1998) classify these stars as CTTS. We thus consider this source as class II.

ROXRF21: (2) ROXR1-43 was identified with GY263 and IRS43 (CMFA). (8) Best value from Grosso et al. (1997). (9) This is the bolometric luminosity (see Grosso et al. 1997).

ROXRF23: (2) ROXR1-46 was identified with an unnamed optical star (CMFA), probably the star B162730-244726. (5) We identified this X-ray with the IR star B162728-244803 just at the border of the X-ray error box.

ROXRF24: (5) This source is red in the PMM USNO-A1.0 Catalogue (Monet et al. 1996) with $B = 20.1$ and $R = 16.3$.

ROXRF25: (2) ROXR1-48 was identified with GY280, GY290, and GY291 (CMFA).

ROXRF28: (5) The IR star B162735-244532:B is also in the 90% confidence error box but its J -band luminosity (> 17) is lower than GY296=B162735-244532:A (12.62).

ROXRF37: (7) The *Hipparcos* distance is 75 pc: this star is a foreground F2V star.

References to Table B.1: B = Barsony et al. (1997). BBRCG = Barsony et al. (1989). DoAr = Dolidze & Arakelyan (1979). El = Elias (1978). GSS = Grasdalen et al. (1973). GY = Greene & Young (1992). HD = The Henry Draper catalogue (Draper 1918). IRS = Wilking et al. (1989). ROXC = Montmerle et al. (1983). ROXs = Bouvier & Appenzeller (1992). S = abbreviation for ‘‘Source’’ in Grasdalen et al. (1973). SKS = Strom et al. (1995; Table 1). SR = Struve & Rudkjøbing (1949). U = The PMM USNO-A1.0 Catalogue (Monet et al. 1996). VSS = Vrba et al. (1976). VSSG = Vrba et al. (1975). WL = Wilking & Lada (1983). WSB = Wilking et al. (1987). YLW = Young et al. (1986).

observation (ROXR1-19, 30, 45, 47, and ROXR2-27, 30, 33). We conclude that the non-detection of the 21 *PSPC* sources by the *HRI* can be fully explained by the difference in sensitivity and intrinsic variability.

We can also compare our detections with *ASCA* (Koyama et al. 1994; Kamata et al. 1997; see observation field in Fig. 1) despite its lower angular resolution. Kamata et al. (1997) detected 19 X-ray sources, of which 10 were

previously observed by Koyama et al. (1994). Compared to *Einstein Observatory* and *ROSAT PSPC* observations, 7 new X-ray sources were discovered by *ASCA*.¹⁸ These 7 X-ray sources are also not detected with the *HRI*. On the 12 sources already observed by *Einstein Observatory*

¹⁸ Note that X-ray source 9B of Kamata et al. (1997) is in fact ROXR1-45 of CMFA.

and *ROSAT PSPC*, we detect 9 sources, the 3 others being below our sensitivity threshold according to the above conversion factor.

Appendix D: Optical/IR counterpart without IR classification

Nine X-ray sources have optical/IR counterpart for which the IR classification is not known. Three of these X-ray sources are found in the *ISOCAM* survey, but with only upper limits in LW2 and LW3 filters. We give here their spectral energy distribution (see Fig. D.1), and discuss their possible IR classification. In case of doubt, the resulting Class II (or Class III) source candidates have not been included in the statistic studies of this article.

ROXRA8: The counterpart of this X-ray source is the optical star Chini8=SKS3 ($R = 16.6$, $K = 9.5$). The *ISOCAM* LW2 and LW3 upper limits exclude an IR excess. We classify this source as a Class III source.

ROXRF12: A weak star is visible in the 90% confidence error box on the DSS2 image, but this star is neither found in the BKL T survey, nor in the PMM USNO-A1.0 catalogue. The low optical/near IR magnitudes imply a low luminosity for this object. We propose this source as a weak Class II or Class III source candidate detected during a strong X-ray flare. This source may also be a brown dwarf.

ROXRF18: The counterpart of this X-ray source is the IR star B162720-243820 ($K = 14.6$). This star is visible in the DSS2 (red) optical image, but it is not in the PMM USNO-A1.0 catalogue (probably because only stars appearing both in blue and red images were accepted), thus we have no estimate of its B and R magnitudes. The low near IR magnitudes imply a low luminosity for this object. This source may be a weak Class II or Class III source candidate detected during a strong X-ray flare. *ISOCAM* LW2 and LW3 upper limits do not exclude an IR excess for this object. This object can also be a weak Class I protostar with a strong X-ray flare.

ROXRF23: The counterpart of this X-ray source is the IR star B162728-244803 ($K = 14.1$; see note in Table B.1). The low near IR magnitudes imply a low luminosity for this object. The SED of this source peaks in the *H*-band. We propose this source as a weak Class II or Class III source candidate detected during a strong X-ray flare.

ROXRF24: The counterpart of this X-ray source is an optical star ($R = 16.3$) named only in the PMM USNO-A1.0 catalogue (Monet et al. 1996). Unfortunately, this object lies outside the BKL T survey. We propose this source as Class II or Class III source candidate.

ROXRF25: The counterpart of this source is BBRG50 observed only in *K*-band ($K = 11.7$). This source is not retrieved in BKL T. The *ISOCAM* LW2 and LW3 upper limits exclude a strong IR excess. We propose this source as Class II or Class III source candidate.

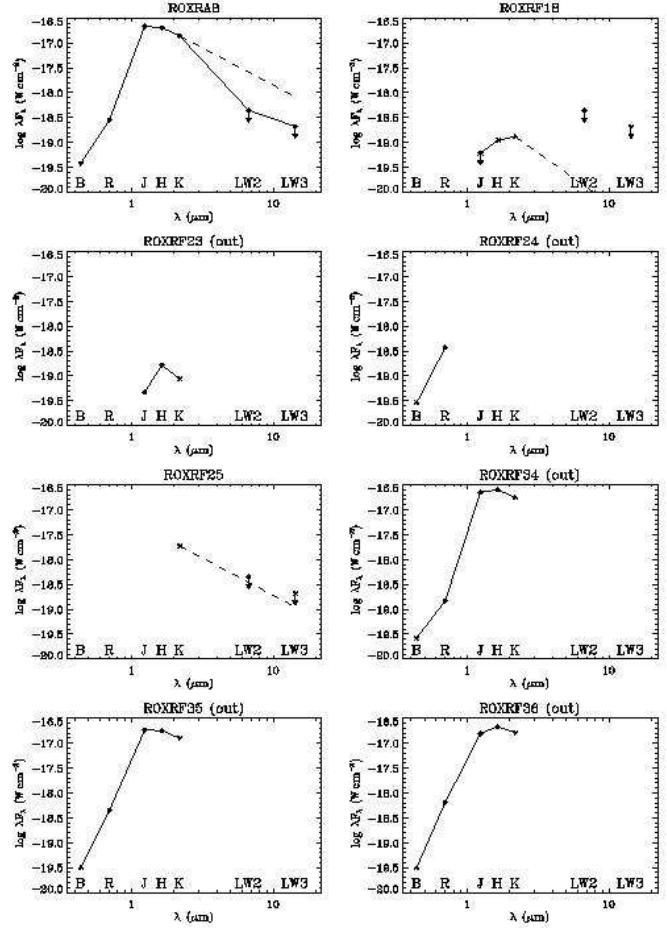


Fig. D.1. Spectral Energy Distribution of optical/IR counterparts without IR classification. B and R data come from the PMM USNO-A1.0 catalogue (Monet et al. 1996); *J*, *H*, *K* data come from BKL T; LW2 and LW3 are the *ISOCAM* upper limit at 10 mJy from Bon-temps et al. (2000). The dashed line shows the limit between Class II source and Class III source classification ($\alpha_{\text{IR}} = d \log(\lambda F_{\lambda}) / d \log \lambda = -1.5$ from AM). “out” means that the source is outside the *ISOCAM* survey.

ROXRF34: The counterpart of this X-ray source is the optical star WSB58=B162800-244819 ($R = 17.3$, $K = 9.3$). Wilking et al. (1987) noted a probable H_{α} detection needing confirmation. The SED of this source peaks in the *H*-band. We propose this source as Class II or Class III source candidate.

ROXRF35: The counterpart of this X-ray source is the optical star B162800-245340 ($R = 16.1$, $K = 9.6$). The SED of this source peaks in the *J*-band. We propose this source as Class II or Class III source candidate.

ROXRF36: The counterpart of this X-ray source is the optical star B162812-245043 ($R = 15.7$, $K = 9.4$), which appears to be a close binary ($\sim 1.5''$) in the second Digitized Sky Survey (see Fig. B.1). The SED of this

source peaks in the H -band. We propose this source as Class II or Class III source candidate.

References

- Abergel, A., et al., 1996, *A&A* 315, L329
- André, P., Montmerle, T., Feigelson, E.D., 1987, *AJ* 93, 1182
- André, P., Montmerle, T., Feigelson, E.D., Stine, P.C., Klein, K.-L., 1988, *ApJ* 335, 940
- André, P., Ward-Thompson, D., Barsony, M., 1993, *ApJ* 406, 122
- André, P., Montmerle, T., 1994, *ApJ* 420, 837 (AM)
- André, P., Ward-Thompson, D., Barsony, M., 2000, in V. Mannings, A.P. Boss, S.S. Russell (eds.), *Protostars and Protoplanets IV*, in press
- Aschwanden, M.J., Dennis, B.R., Benz, A.O., 1998, *ApJ* 497, 972
- Barsony, M., Carlstrom, J.E., Burton, M.G., Russell, A.P.G., Garden, R., 1989, *ApJ* 346, L93
- Barsony, M., Kenyon, S.J., Lada, E.A., Teuben, P.J., 1997, *ApJS* 112, 109 (BKLT)
- Bontemps, S., et al., 1998, in *ASP Conf. Ser. 132: Star Formation with the Infrared Space Observatory*, 141
- Bontemps, S., et al., 2000, *A&A*, submitted
- Bouvier, J., Appenzeller, I., 1992, *A&AS* 92, 481
- Canzian, B., 1997, *CCD Astronomy* 4, 16
- Casanova, S., 1994, Ph.D. thesis, Paris VI University
- Casanova, S., Montmerle, T., Feigelson, E.D., André, P., 1995, *ApJ* 439, 752 (CMFA)
- Chen, H., Myers, P.C., Ladd, E.F., Wood, D.O.S., 1995, *ApJ* 445, 377
- Chini, R., 1981, *A&A* 99, 346
- Comerón, F., Rieke, G.H., Burrows, A., Rieke, M.J., 1993, *ApJ* 416, 185
- Cruddace, R.G., Hasinger, G.R., Schmitt, J.H., 1988, in *Astronomy from Large Databases*, 177
- Dahlem, M., et al., 1999, *XMM Users' Handbook*, ESA/ESTEC
- David, L.P., Harnden, F.R., Kearns, K.E., Zombeck, M.V., 1997, *The ROSAT HRI Calibration Report*, U.S. ROSAT Science Data Center/SAO
- de Geus, E.J., Bronfman, L., Thaddeus, P., 1990, *A&A* 231, 137
- de Zeeuw, P.T., Hoogerwerf, R., de Bruijne, J.H.J., Brown, A.G.A., Blaauw, A., 1999, *AJ* 117, 354
- Dolidze, M.V., Arakelyan, M.A., 1979, *SvA* 3, 434
- Draper, H., 1918, *Ann. Astron. Obs. Harvard Coll.*, 91
- Elias, J.H., 1978, *ApJ* 224, 453
- Feigelson, E.D., Nelson, P.I., 1985, *ApJ* 293, 192
- Feigelson, E.D., Casanova, S., Montmerle, T., Guibert, J., 1993, *ApJ* 416, 623
- Feigelson, E.D., 1996, *ApJ* 468, 306
- Feigelson, E.D., Montmerle, T., 1999, *ARA&A* 37, 363 (FM)
- Fleming, T.A., Gioia, I.M., Maccacaro, T., 1989, *ApJ* 340, 1011
- Grasdalen, G.L., Strom, K.M., Strom, S.E., 1973, *ApJ* 184, L53
- Greene, T.P., Young, E.T., 1992, *ApJ* 395, 516 (GY)
- Greene, T.P., Wilking, B.A., André, P., Young, E.T., Lada, C.J., 1994, *ApJ* 434, 614 (GWAYL)
- Greene, T.P., Meyer, M.R., 1995, *ApJ* 450, 233
- Greene, T.P., Lada, C.J., 1996, *AJ* 112, 2184
- Grosso, N., Montmerle, T., Feigelson, E.D., André, P., Casanova, S., Gregorio-Hetem, J., 1997, *Nat* 387, 56
- Guillout, P., Haywood, M., Motch, C., Robin, A.C., 1996, *A&A* 316, 89
- Jensen, E.L.N., Mathieu, R.D., 1997, *AJ* 114, 301
- Kamata, Y., Koyama, K., Tsuboi, Y., Yamauchi, S., 1997, *PASJ* 49, 461
- Knude, J., Høg, E., 1998, *A&A* 338, 897
- Koyama, K., 1987, *PASJ* 39, 245
- Koyama, K., Asaoka, I., Kuriyama, T., Tawara, Y., 1992, *PASJ* 44, L255
- Koyama, K., Maeda, Y., Ozaki, M., Ueno, S., Kamata, Y., Tawara, Y., Skinner, S., Yamauchi, S., 1994, *PASJ* 46, L125
- Lada, C.J., Wilking, B.A., 1984, *ApJ* 287, 610
- Lada, C.J., 1987, in *IAU Symp. 115: Star Forming Regions*, Vol. 115, 1
- Lavalley, M., Isobe, T., Feigelson, E., 1992, in *ASP Conf. Ser. vol. 25: Astronomical Data Analysis Software and Systems I*, Vol. 1, 245
- Lawson, W.A., Feigelson, E.D., Huenemoerder, D.P., 1996, *MNRAS* 280, 1071
- Leous, J.A., Feigelson, E.D., André, P., Montmerle, T., 1991, *ApJ* 379, 683
- Loren, R.B., 1989, *ApJ* 338, 902
- Loren, R.B., Wootten, A., Wilking, B.A., 1990, *ApJ* 365, 269
- Luhman, K.L., Rieke, G.H., 1999, *ApJ* 525, 440
- Martín, E.L., 1997, *A&A* 321, 492
- Martín, E.L., Montmerle, T., Gregorio-Hetem, J., Casanova, S., 1998, *MNRAS* 300, 733
- Monet, D., et al., 1996, *USNO-SA1.0 catalogue*, U.S. Naval Observatory, Washington DC
- Montmerle, T., Koch-Miramond, L., Falgarone, E., Grindlay, J.E., 1983, *ApJ* 269, 182
- Montmerle, T., Feigelson, E.D., Bouvier, J., André, P., 1993, in *Protostars and Planets III*, 689
- Montmerle, T., 1996, in *ASP Conf. Ser. 109: Ninth Cambridge Workshop on Cool Stars, Stellar Systems, and the Sun*, Vol. 9, 405
- Montmerle, T., Grosso, N., Tsuboi, Y., Koyama, K., 2000, *ApJ* 532, 1097
- Morrison, R., McCammon, D., 1983, *ApJ* 270, 119
- Neuhäuser, R., Sterzik, M.F., Schmitt, J.H.M.M., Wichmann, R., Krautter, J., 1995, *A&A* 297, 391
- Neuhäuser, R., Briceño, C., Comerón, F., Hearty, T., Martín, E.L., et al., 1999, *A&A* 343, 883
- Nordh, L., et al., 1996, *A&A* 315, L185
- Palla, F., Stahler, S.W., 1999, *ApJ* 525, 772
- Preibisch, T., Zinnecker, H., Herbig, G.H., 1996, *A&A* 310, 456
- Prestwich, A.H., Silverman, J., Mc Dowell, J., Callanan, P., Snowden, S., 1998, *Spectral Calibration of the ROSAT HRI*, U.S. ROSAT Science Data Center/SAO
- Rosner, R., Vaiana, G.S., 1978, *ApJ* 222, 1104
- Ryter, C.E., 1996, *Ap&SS* 236, 285
- Stine, P.C., Feigelson, E.D., André, P., Montmerle, T., 1988, *AJ* 96, 1394
- Strom, K.M., Kepner, J., Strom, S.E., 1995, *ApJ* 438, 813 (SKS)
- Struve, O., Rudkjöbing, M., 1949, *ApJ* 109, 92
- Vrba, F.J., Strom, S.E., Strom, K., Grasdalen, G.L., 1975, *ApJ* 197, 77
- Vrba, F.J., Strom, S.E., Strom, K., 1976, *AJ* 81, 958

- Walter, F.M., Vrba, F.J., Mathieu, R.D., Brown, A., Myers, P.C., 1994, AJ 107, 692
- Ward-Thompson, D., 1993, MNRAS 265, 493
- Wilking, B.A., Lada, C.J., 1983, ApJ 274, 698
- Wilking, B.A., Schwartz, R.D., Blackwell, J.H., 1987, AJ 94, 106
- Wilking, B.A., Lada, C.J., Young, E.T., 1989, ApJ 340, 823
- Wilking, B.A., 1992, in ESO Sci. Rep. 11: Low Mass Star Formation in Southern Molecular Clouds, 159
- Young, E.T., Lada, C.J., Wilking, B.A., 1986, ApJ 340, 823
- Zimmermann, H.U., et al., 1997, EXSAS User's Guide, MPE Report, ROSAT Scientific Data Center, Garching